

This is the peer reviewed version of the following article:

Rusmirović, Jelena D., Nina Obradović, Jovana Perendija, Ana Umićević, Ana Kapidžić, Branislav Vlahović, Vera Pavlović, Aleksandar D. Marinković, and Vladimir B. Pavlović. 2019. “Controllable Synthesis of Fe₃O₄-Wollastonite Adsorbents for Efficient Heavy Metal Ions/Oxyanions Removal.” *Environmental Science and Pollution Research*. <https://doi.org/10.1007/s11356-019-04625-0>.



This work is licensed under a [Creative Commons Attribution Non Commercial No Derivatives 4.0](https://creativecommons.org/licenses/by-nc-nd/4.0/) license

[Click here to view linked References](#)

Controllable Synthesis of Fe₃O₄-Wollastonite Adsorbents for Efficient Heavy Metal Ions/Oxyanions Removal

Jelena D. Rusmirović^{1*}, Nina Obradović², Jovana Perendija³, Ana Umičević⁴, Ana Kapidžić⁴, Branislav Vlahović⁵, Vera Pavlović⁶, Aleksandar D. Marinković⁷, Vladimir B. Pavlović^{2,8}

¹*Innovation Center of the Faculty of Technology and Metallurgy, University of Belgrade, Karnegijeva 4, 11120 Belgrade, Serbia, jrusmirovic@tmf.bg.ac.rs*

²*Institute of Technical Sciences of SASA, Knez Mihailova 35/IV, 11000 Belgrade, Serbia*

³*Institute of Chemistry, Technology and Metallurgy, University of Belgrade, Njegoševa 4, 11000, Serbia*

⁴*Vinča Institute of Nuclear Sciences, University of Belgrade, Serbia*

⁵*North Carolina Central University, Department of Mathematics and Physics, Durham, United States*

⁶*Faculty of Mechanical Engineering, Kraljice Marije 16, 11120 Belgrade, Serbia*

⁷*Faculty of Technology and Metallurgy, University of Belgrade, Karnegijeva 4, 11120 Belgrade, Serbia*

⁸*Faculty of Agriculture, University of Belgrade, Nemanjina 6, 11080 Belgrade-Zemun, Serbia*

***Corresponding author:** Jelena Rusmirović, Innovation Center of the Faculty of Technology and Metallurgy, University of Belgrade, Karnegijeva 4, 11120 Belgrade, Serbia, jrusmirovic@tmf.bg.ac.rs

Abstract

Iron oxide, in the form of magnetite (MG), functionalized porous wollastonite (WL) was used as an adsorbent for heavy metal ions (cadmium and nickel) and oxyanions (chromate and phosphate) removal from water. The porous WL was synthesized from calcium carbonate and siloxane by controlled sintering process using low molecular weight submicro-sized poly(methyl methacrylate) as a pore-forming agent. The precipitation of MG nanoparticles was carried out directly by a polyol-medium solvothermal method or *via* branched amino/carboxylic acid cross-linker by solvent/nonsolvent method producing WL/MG and WL- γ -APS/MG adsorbents, respectively. The structure/properties of MG functionalized WL was confirmed by applying FTIR, Raman, XRD, Mössbauer, and SEM analysis. Higher adsorption capacities of 73.126, 66.144, 64.168 and 63.456 mg g⁻¹ for WL- γ -APS/MG in relation to WL/MG: 55.450, 52.019, 48.132 and 47.382 mg g⁻¹ for Cd²⁺, Ni²⁺, phosphate and chromate, respectively, were obtained using non-linear Langmuir model fitting. Adsorption phenomena were analyzed using monolayer statistical physics model for single adsorption with one energy. Kinetic study showed exceptionally higher pseudo second-order rate constants for WL- γ -APS/MG, e.g. 1.17 – 13.4 times, with respect to WL/MG indicating importance of both WL surface modification and controllable precipitation of MG on WL- γ -APS.

Keywords Calcium metasilicates ceramic; Magnetite functionalization; Solvent/nonsolvent method; Polyol-thermal method; Heavy metals; Adsorption; Fe₃O₄.

Introduction

Rapid global industrialization increases the amount of effluent consisted of chemical wastes such as volatile organic compounds (industrial solvents), heavy metals and oxyions, pharmaceutical drugs and their metabolites, *etc.* Industrial effluents are one of the prime sources of environmental toxicity that deteriorates water quality (Paul 2017). Long-term exposure to heavy metals, such as cadmium, nickel and chromium (Cd^{2+} , Ni^{2+} and Cr(VI)), by ingestion/inhalation leads to a buildup in kidneys and possible kidney disease, lung damage, cancer, and fragile bones (Karthikeyan et al. 2005; Martin and Griswold 2009). Due to that, Environmental Protection Agency (EPA) limits concentration of Cd^{2+} to 0.005 ppm and of Ni^{2+} and Cr(VI) to 0.1 ppm in water (EPA 2014). As an essential nutrient required for critical biological reactions maintaining the normal homeostatic control of the cell, and growth of algae phosphorus is an important component of different cellular structures (Mezenner and Bensmaili 2009; Razaque 2011). The phosphorus concentration has to be limited in order to control algal blooming (Mezenner and Bensmaili 2009). The phosphate discharge standard of wastewater is averaged on 1–2 ppm in order to satisfy the stringent EPA's limit of phosphorous concentration in natural water (0.02 ppm) (Rout et al. 2015, 2016). With the aim to maintain the pollutant concentration within the permissible limits, purification/pollutant removal from industrial water becomes imposed as a solution for susceptibility environmental toxicity.

In recent years, a great attention was directed in development of physically and chemically removing of heavy metals from contaminated water by a variety of methods, including membrane separation, flocculation, adsorption, ion-exchange, precipitation, evaporation, and electrolysis (D'Halluin et al. 2017; Iannazzo et al. 2017; Han et al. 2018). Due to low operational cost and high efficient in the removal of many heavy metal ions, as well as possibility of using natural materials as adsorbents, the adsorption stands out as one of the most efficient and widely used techniques for removing of metal ions (Zeng et al. 2015). Development of the more effective and cheaper adsorbents, that may be of mineral, organic or biological origin has been studied in the recent decade (Abdel-Halim and Al-Deyab 2011; Zeng et al. 2015). Calcium silicates have received considerable attention as adsorbent for heavy metal adsorption due to their excellent bioactivity and biocompatibility (Chen et al. 2008; Zhao et al. 2014). Wollastonite (WL) is a naturally occurring and cheap α -calcium metasilicate ($\alpha\text{-CaSiO}_3$) that is commonly used in preparing ceramic bodies and other materials, but lately have used as an adsorbent in water pollution control (Sharma et al. 1990b, a, 2007; Sharma 2001; Obradović et al. 2017a). Calcium oxide (CaO) and silicon dioxide (SiO_2) are the main constituents of WL ($\text{CaO/SiO}_2=48.18\%/48.52\%$ by weight) that can be responsible for heavy metals adsorption (Sharma 2001). Sharma et al. were investigated ability of natural WL to remove Cd^{2+} , Ni^{2+} and Cr(VI) ions from water and found maximum removal of 93.6% and 69.5% for Cd^{2+} and Cr(VI) ions, respectively, and maximum adsorption capacity of 6.52 mg g^{-1} for Ni^{2+} ions (Sharma et al. 1990b, a, 2007). The main disadvantage of WL for use as an adsorbent for the removal of pollutants from aquatic systems is the hydrophilicity of its surface. Surface modification, as a key process in functional WL preparation, renders hydrophilic WL surface hydrophobic (Ding et al. 2011). In order to reduce the hydrophilicity of the WL surface and, therefore, increase the heavy metals ions adsorption capacity, it is necessary to functionalize its surface.

1
2
3
4 Iron oxides and oxidehydroxides based adsorbents have been widely used in water treatment
5 systems for the removal of ionic pollutants (Markovski et al. 2014b, a, Taleb et al. 2015, 2016a;
6 Lin et al. 2017; Zeng et al. 2017). Due to expressed electrostatic attraction and ligand exchange
7 with heavy metal ions, magnetite (MG – Fe₃O₄) nanoparticles were shown to be highly efficient
8 materials for heavy metal ion removal by adsorption (Kalantari et al. 2014). Besides, using of
9 MG in production hybrid adsorbents resolve separation problems because, due to their magnetic
10 property, MG particles can be easily separated from aqueous solutions using an external
11 magnetic field(Kalantari et al. 2014). Moreover, amination of MG surface helps in formation of
12 uniform Fe₃O₄ deposit without appreciable nanoparticle aggregation. In that way, improvement
13 of two benefit was achieved: controllable MG precipitation due to the strong metal chelation of
14 amine groups and improved adsorption performances of the obtained adsorbent (Qi et al. 2017).
15 To the best of our knowledge, there are no examples in the literature dealing with the removal of
16 Cd²⁺, Ni²⁺, chromate and phosphate ions by WL based adsorbent with impregnated MG particles.
17
18
19
20

21 Besides the adsorbent morphology and surface properties, the operating conditions play an
22 important role in achieved high adsorption capacities. Many theoretic studies (isothermal,
23 kinetic, statistical-physic models) are carried out to understand the behavior of single-compound
24 adsorption systems since the operating conditions can be potentially infinite in terms of
25 combination of pollutant concentration, temperature and time of the pollutant/adsorbent
26 contact(Sellaoui et al. 2016a, b, 2017a, b). Freundlich and Langmuir models are mostly used to
27 analyze the adsorption equilibrium of heavy metal removal using WL or MG based adsorbents in
28 a single component system(Sharma et al. 1990b, a, 2007; Taleb et al. 2016b; Obradović et al.
29 2017b, a). More precise interpretation of single adsorption isotherms can be obtained using
30 statistical physic theory, etc. monolayer models with one or two energies. The obtained
31 theoretical results connect experimental result with successfulness of the applied adsorbent
32 synthesis process and operation conditions.
33
34
35

36 In the present work, the ability of a hybrid material consisting of the WL as a support of MG
37 particles, for removal of Cd²⁺, Ni²⁺, chromate and phosphate ions from aqueous solutions was
38 studied. The ions adsorption capacity of the WL impregnated with MG can be controlled either
39 by directly precipitation of MG particles or polyol-medium solvothermal method and *via* (3-
40 aminopropyl)trimethoxy-silane cross-linker by solvent/nonsolvent system method. The
41 adsorption experiments were performed in order to analyze the influence of the MG precipitation
42 method, adsorbent amount, adsorption temperature and contact time on achieved capacities.
43 Moreover, the present work is a modeling study of heavy metals ion/oxyanions removal and
44 provides useful information about the adsorption mechanisms in single-compound system.
45
46
47
48
49

50 **Experimental section**

53 **Materials**

54 All reagents were of analytical grade and used without purification. Deionized water (DW), of
55 resistivity of 18 MΩcm, was used. Ultra-pure HNO₃ acid and diethylene-triaminepentaacetic
56 acid (DETAPAA) were supplied from Fluka. Iron(III) chloride hexahydrate (FeCl₃·6H₂O),
57 iron(II) sulphateheptahydrate (FeSO₄·7H₂O), sodium hydrogen carbonate (NaHCO₃), sodium
58 acetate (NaAc), polyethylene glycol 6000 (PEG-6000), (3-aminopropyl)triethoxysilane,
59
60
61
62
63
64
65

1
2
3
4 methanol, methyl methacrylate (MMA), potassium persulphate, calcium carbonate (CaCO₃),
5 *N,N*-dimethylformamide (DMF), toluene and isopropyl alcohol were supplied from Sigma-
6 Aldrich. Methylhydro-cyclosiloxane was supplied from abcr GmbH. Standard solutions of
7 nickel(II) nitrate hexahydrate (1000 ppm) was supplied from Accustandard. Cadmium(II) nitrate
8 tetrahydrate (1000 ppm) was supplied from Panreac. Chromium(VI) standard for ICP
9 (1000 ppm) was supplied from Sigma-Aldrich. Phosphate standard solution (1000 pm) was
10 supplied from Merck KGaA.
11
12

13 **Synthesis of submicropoly(methyl methacrylate) spheres**

14 Synthesis of submicro poly(methyl methacrylate) spheres (PMMA) was done according to the
15 procedure described elsewhere (Shim et al. 2004). Polymerization was carried out in a 250 ml
16 three-necked glass reactor equipped with a magnetic stirrer (stirring rate 100 rpm), reflux
17 condenser, nitrogen inlet tube and an oil bath. Mixture of 100 ml of methanol and 50 ml water
18 was added in the glass reactor and followed by addition of 5 g of MMA and the temperature was
19 raised up to 70 °C. Thereafter, the aqueous potassium persulphate (KPS) solution (0.0375 g of
20 KPS in 10 ml of water) was added and the polymerization was initiated under nitrogen (inert)
21 atmosphere at 70 °C. After 1 h, the mixture was cooled down using an ice-bath and PMMA was
22 washed three times with a cold methanol/water mixture (90/10 v/v) by applying repeated
23 centrifugation/ultrasound treatment.
24
25
26
27

28 **Synthesis of diethylenetriaminepentaacetic acid dianhydride**

29 Synthesis of diethylenetriaminepentaacetic acid dianhydride (DETAPADA) was done according
30 to the procedure described elsewhere (Capretta et al. 1995). In a dry three-necked glass reactor
31 equipped with a magnetic stirrer, reflux condenser, nitrogen inlet tube and calcium chloride
32 protection tube, immersed in an oil bath, 23.6 g of DETAPAA (60.0 mmol) was suspended in
33 31 ml of dry pyridine followed by addition of 24 ml of acetic anhydride. The mixture was heated
34 at 65 °C for 24 h under intensive mixing, cooled down and filtered under vacuum and inert
35 atmosphere. The obtained product, white solid, was collected and washed with 200 ml of acetic
36 anhydride and 200 ml of diethyl ether and dried under vacuum at 50 °C for 6 h.
37
38
39

40 **Synthesis of wollastonite based adsorbent**

41 Wollastonite-based adsorbents were synthesized in a two-step pressureless sintering process
42 described in the previous research (Obradović et al. 2017a). In the first step 7.79 g methylhydro-
43 cyclosiloxane was dissolved in 100 ml of isopropyl alcohol under magnetic stirring at ambient
44 temperature. Thereafter, 9.00 g of micro-sized CaCO₃ was added and mixed for 10 min, followed
45 by ultrasound treatment (*Bandelin electronic ultrasonic bath, Berlin, Germany, power 120 W,*
46 *frequency 35 kHz*) for 20 min and dried overnight at 80 °C. The obtained paste was calcined in a
47 furnace at 250 °C during 30 min, with a 5 °C/min heating rate. In the second step, the as-prepared
48 wollastonite powder (0.80 g) was carefully homogenized with a pore-forming agent (0.20 g
49 submicro PMMA spheres), molded in a cylinder pallet (dimension 5 mm·φ10) and sintered at
50 900 °C during 1 h, with a 5 °C/min heating rate.
51
52
53

54 **Direct attaching of MG spheres on wollastonite**

55 The generation of MG nanoparticles was carried out by a polyol-medium solvothermal method
56 according to the literature description (Wang et al. 2011). In single necked glass reactor of 50 ml,
57 0.405 g of FeCl₃·6H₂O was dissolved into 20 ml ethylene glycol, producing an orange solution.
58 1.0 g of sintered wollastonite was homogeneously dispersed applying sonication for 3 h.
59 Addition of NaAc (1.8 g) and PEG-6000 (0.5 g), keeping a constant mechanical stirring at 800
60
61
62
63
64
65

rpm for 30 min, provided pH and viscosity adjustment of the dispersion. The obtained viscous product was transferred in a Teflon-lined stainless steel autoclave of a 80 ml capacity followed by heating at 200 °C for 8 h. The black precipitates, obtained after cooling the reaction mixture, were washed with water and ethanol three times and dried in a vacuum oven at 60 °C. The final product was labeled WL/MG.

Attachment of MG nanoparticles on branched carboxyl functionalized wollastonite

Stepwise synthesis of amino-functionalized and subsequently carboxy terminal functionalization of WL was performed by applying the modified literature method (Taleb et al. 2015). Amino group functionalization of WL was achieved by a direct silanization of WL with (3-aminopropyl)triethoxysilane (γ -APS). The product was named WL- γ -APS. In a three-necked glass reactor of 100 ml, equipped with a magnetic stirrer, reflux condenser, nitrogen inlet tube and an oil bath for heating, 1.0 g of WL was dispersed into 50 ml of toluene under continuous stirring, then 1.0 ml of triethylamine and 1.0 ml of γ -APS were added into the suspension, and followed by refluxing at 80 °C for 12 h under a nitrogen atmosphere. WL- γ -APS was purified by washing in ethanol, dried under vacuum at 60 °C and then used for carboxylic acid modification in order to obtain more reactive centers for MG precipitation. The quantitative Kaiser test (Sarin et al. 1981) predicted the concentration of terminal amino functions present on the WL- γ -APS material to be 2.50 mmol g⁻¹. Modified WL- γ -APS (1.2 g) was dispersed in 10 ml of DMF under stirring, and after 10 ml of 0.1 mol l⁻¹ solution of DETAPADA was added into the suspension, and mixed at room temperature for 24 hrs. Finally, the product (WL/DA) was dried under vacuum at 60 °C and used for attaching of MG spheres according to the procedure described elsewhere in the literature (Taleb et al. 2015). The acidic site concentrations were determined using the Boehm titration method (Boehm 1994), and the determined acid value for WL/DA was found to be 4.3 mmol g⁻¹.

In the last step, WL/DA (1.3 g) was sonicated in 30 ml of toluene with simultaneous introduction of nitrogen for 30 min, and after pH of dispersion was adjusted at ~6. The reaction was continued by drop-wise addition of 1.0 ml of 0.125 mol l⁻¹ FeSO₄·7H₂O solution for 15 min under magnetic stirring and inert atmosphere. Neutralization of the reaction mixture with a 1 mol l⁻¹ NaHCO₃ buffer solution cause precipitation of iron oxide in the MG form. The reaction took place by heating at 90 °C for 48 h while a black product was obtained. The obtained product was filtered, washed with 200 ml DW and dried applying vacuum/drying treatment at 60 °C/2000 Pa for 6 hours. The final product was named WL- γ -APS/MG. Schematic illustration of WL modification methods is shown in Fig. 1.

Fig. 1.

Adsorption and kinetic experiments

Batch adsorption experiments of Cd²⁺, Ni²⁺, Cr(VI) and phosphate ions removal, under mixing using a laboratory shaker (*Digital Heating Shaking Drybath* by Thermo SCIENTIFIC), were applied to determine adsorption capacities and investigate effects of diffusional processes on the performance of synthesized adsorbents. An appropriate adsorbent mass ($m = 1.0, 1.5, 2.5, 5.0, 7.5$ and 10 mg), was placed in glass vials containing 10 ml of the standard solutions of ions of interest (Cd²⁺, Ni²⁺, Cr(VI) and phosphate ions) at initial concentrations, C_i , of 10 ppm.

1
2
3
4 According to the determined values of the point of zero charge of the WL based adsorbents and
5 the ion distribution, the pH values of the solutions of Cd²⁺ and Ni²⁺ ions were set at 7.5 and for
6 the solutions of Cr(VI) and phosphate ions were set at 6.5. The adsorption and kinetic
7 experiments were performed at 298, 308 and 318 K. The adsorption kinetic was studied by
8 varying the adsorbent/ion contact time in the range 5-90 min at C_i=10 ppm. The adsorption
9 capacities of Cd²⁺, Ni²⁺, Cr(VI) and phosphate ions removal using WL based adsorbents were
10 calculated according to the following Eq. (1):
11
12

$$13 \quad q = \left(\frac{C_i - C_f}{m} \right) V \quad (1)$$

14
15
16
17 Where q is the adsorption capacity in mg g⁻¹, C_i and C_f are the initial and final concentrations of
18 ions in ppm, V is the volume of solution in l, and m is the mass of the adsorbent in g. After
19 adsorption experiments, WL/MG and WL- γ -APS/MG adsorbents were washed with DW.
20 Further, in order to evaluate the adsorbent regeneration capabilities, wet adsorbents were
21 redispersed in 20 ml of solution for regeneration (NaOH/NaCl, 0.5/0.5 mol l⁻¹) (Taleb et al.
22 2016b). The amount of desorbed ions in effluent water was measured after mixing by the
23 laboratory shaker for 3 h in a batch system. Three consecutive adsorption/desorption cycles were
24 performed.
25
26
27

28 **Characterization method**

29 Fourier transforms infrared spectroscopy (FTIR) spectra of the WL based adsorbents were
30 recorded in the absorbance mode using a Nicolet™ iS™10 FT-IR Spectrometer (Thermo Fisher
31 SCIENTIFIC) with Smart iTR™ Attenuated Total Reflectance (ATR) Sampling accessories,
32 within the range of 400-4000 cm⁻¹, at a resolution of 4 cm⁻¹ and in 32 scan mode.
33
34

35 The X-ray powder diffraction patterns were obtained using a Philips PW-1050 diffractometer
36 with λ Cu-K α radiation and a step/time scan mode of 0.05 ° s⁻¹. The measurements were taken at
37 room temperature in air.
38

39 The morphology of the sintered powders was characterized by the scanning electron microscopy
40 (JEOL JSM-6390 LV). The pellets were crushed and covered with gold in order to perform these
41 measurements.
42
43

44 Raman spectra of the WL-based adsorbent, recorded in the range 200–1200 cm⁻¹, were collected
45 with a Horiba JobinYvon Aramis Raman/PL System. The system employed a 633 nm laser
46 (output power 4 mW, on sample 1 mW). All the measurements were realized using a
47 spectrometer equipped with 1800 lines mm⁻¹, microscope objective of x100 and acquisition of
48 10s per 30 cycles.
49
50

51 The ⁵⁷Fe-Mössbauer spectra were obtained at room temperature in the standard transmission
52 geometry in the constant acceleration mode using a ⁵⁷Co(Rh) radioactive source. The velocity
53 scale was calibrated by the spectrum of alpha iron foil. The Mössbauer spectra were fitted by
54 WinNormos software package (Brand 2008). The isomer shift values (δ) are given relative to α -
55 Fe ($\delta = 0$).
56
57
58
59
60
61
62
63
64
65

1
2
3
4 The Cd²⁺, Ni²⁺, Cr(VI) and phosphate ions concentrations in the solutions after the adsorption
5 and kinetic experiments were analyzed by a PinAAcle 900T Atomic Absorption Spectrometer.
6 The mean value from three adsorption experiments was used for processing of experimental data.
7
8
9

10 **Results and discussion**

14 **ATR-FTIR analysis**

15 ATR-FTIR spectra of the unmodified and MG modified WL-based adsorbents are shown in Fig.
16 2. The bands characteristic for WL containing ceramics observed at 994 cm⁻¹, 1110 cm⁻¹
17 originate from stretching bridging Si–O(Si) vibrations, while bands at 897 cm⁻¹, 874 cm⁻¹, and
18 846 cm⁻¹ originates from stretching non-bridging Si–O vibrations (Obradović et al. 2017a). The
19 low intensity band at 714 cm⁻¹ originates from stretching vibration of Si–O(Si) bridging bond,
20 which is characteristic for the presence of a 3-membered ring in WL ceramics. The intense band
21 at 1410 cm⁻¹ is assigned to the carbonate ion vibrational modes in bulk calcite. Broad band
22 around 3300-3500 cm⁻¹, observed in ATR-FTIR spectra of WL/DA, originates from hydroxyl
23 group (OH) stretching vibration. The bands at 2930 cm⁻¹ and 2870 cm⁻¹ originate from symmetric
24 and asymmetric stretching vibrations of methylene group. Moreover, the absorption peaks at
25 1680 cm⁻¹ and 1580 cm⁻¹ originates from amide I stretching vibrations, and N-H deformation
26 vibrations coupled with $\nu(\text{C-N})$ vibrations (amide II), respectively.
27
28
29
30

31 The low intensity peak around 564 cm⁻¹ observed in the ATR-FTIR spectrum of WL/MG and
32 WL- γ -APS/MG originates from vibration of the Fe²⁺–O²⁻ functional group (Khalil 2015)
33 overlapped with the peaks which originate from the C=C=O and C-N-C vibrations (DETAPA
34 moiety in WL- γ -APS/MG sample). Raman spectroscopy and ⁵⁷Fe-Mössbauer analysis are more
35 suitable techniques for quantification of the amount of MG doped on WL containing ceramics, as
36 well as the determination of the phase and composition of the deposit.
37
38
39

40 **Fig. 2.**

42 **Raman analysis**

43 Raman spectra of the unmodified and modified (direct/via γ -APS/DA cross-linker) WL based
44 adsorbents are shown in Fig.3. In the Raman spectrum of unmodified WL peaks that originate
45 from both bare WL and β -larnite are noticed. The peak assignment is done according to the
46 literature data and it is shown in Fig.3 (Swamy et al. 1997; Richet et al. 1998; Ricciardi et al.
47 2009; Sokol et al. 2015). The small intensity peak at 1083 cm⁻¹ indicates that there are residual
48 CaCO₃ in WL structure(White 2009; Ricciardi et al. 2009).
49
50
51
52

53 In the Raman spectra of both modified WL samples, *i.e.* WL/MG and WL- γ -APS/MG, two wide
54 peaks of magnetite, followed by two low intensity peaks of maghemite, are observed(de Faria et
55 al. 1997; Ovsyannikov et al. 2010; Li et al. 2012). Partial transformation of magnetite into
56 maghemite is found to induced by laser excitation (de Faria et al. 1997). The WL peaks at <
57 500 cm⁻¹ can be assigned to the Ca-O stretching (the lowest frequencies in the region) and
58 bending vibrations (higher frequencies in the region). On the other hand, Raman signals of WL
59 observed between 500 and 600 cm⁻¹ originate from the O-Si-O bending vibrations. Although the
60
61
62
63
64
65

1
2
3
4 band at 635 cm^{-1} can be attributed to the Si-O-Si bending vibration (Osticioli et al. 2009; Buzatu
5 and Buzgar 2010; Ebbert et al. 2014), some authors point out that this peak originates from the
6 Si-O_{br} stretching vibrations, where O_{br} presents bridging oxygen. The stretching Si-O_{br} vibrations
7 induce also the occurrence of the peak between 650 and 750 cm^{-1} , while Raman peaks between
8 850 and 200 cm^{-1} can be assigned to the Si-O nonbridging stretching vibrations (Si-O_{nbr}).
9
10

11
12 **Fig. 3.**
13

14 **XRD analysis**

15 XRD patterns of sintered unmodified WL and modified WL samples, WL/MG and WL- γ -
16 APS/MG, are presented in Fig.4. All obtained intensities are identified by JCPDS cards (042-
17 0547 for wollastonite CaSiO_3 , and 077-0409 for larnite Ca_2SiO_4). A two-phase system is
18 detected in unmodified WL samples: wollastonite and larnite (13.4 % CaSiO_3 and 86.6 %
19 Ca_2SiO_4). Peaks for magnetite, marked by their indices [(111), (220), (311), (400), (422), (511),
20 (440)] (Wang et al. 2009; Huang et al. 2017), are observed in XRD curves for both WL/MG and
21 WL- γ -APS/MG samples. No additional peaks are observed.
22
23

24
25 **Fig.4.**
26

27 **^{57}Fe -Mössbauer spectroscopy**

28 The ^{57}Fe -Mössbauer spectra of modified WL samples, W- γ -APS/MG and W-MG, are presented
29 in Fig.5. The samples were evaluated using WinNormos-DIST program. The two absorption
30 lines (so called a doublet) were visible in the WL- γ -APS/MG spectrum. The spectrum was fitted
31 with the distribution of the quadrupole splitting. The distribution was described using histogram
32 distribution of 30 doublets of Lorentzian lines with the same FWHM (0.3 mms^{-1}) in steps of
33 0.1 mms^{-1} . The linear correlation between the quadrupole splitting and the isomer shift was
34 applied. Isomer shifts for the quadrupole distribution covered range from ~ 0.33 to $\sim 0.34\text{ mms}^{-1}$.
35 The quadrupole splitting distribution $P(\Delta)$ of the WL- γ -APS/MG sample is presented in Fig.6. In
36 the WL/MG spectrum, besides the dominant central doublet, a broad six-lines absorption feature
37 (so called a sextet) representing the magnetic contribution to the spectrum was also visible. The
38 spectrum was fitted with one discrete doublet and one distribution of the hyperfine magnetic
39 field (distribution of the magnetic splitting). The distribution of the magnetic splitting was
40 described using a histogram distribution of 35 sextets of Lorentzian lines with the same FWHM
41 (0.5 mms^{-1}) from 15 T in steps of 1 T. The linear correlation between the hyperfine magnetic
42 field and the isomer shift was applied. Isomer shifts for the magnetic distribution covered the
43 range from ~ 0.32 to $\sim 0.64\text{ mms}^{-1}$. The quadrupole shift was fixed to zero. The hyperfine
44 magnetic field distribution $P(B_{\text{hf}})$ of the magnetic part of the WL/MG sample is presented in Fig.
45 7. In the same DIST program, one discrete doublet was combined with the magnetic distribution.
46 The ^{57}Fe -Mössbauer parameters of the WL/MG and WL- γ -APS/MG samples are presented in
47 Table 1. Under the assumption that f -factors of Fe atoms at various sites in the particular sample
48 are identical, the area of the corresponding Mössbauer subspectrum was used to access the
49 relative fractions of iron atoms at different sites.
50
51
52
53
54
55

56
57 **Fig. 5.**
58

59 **Fig. 6.**
60
61
62
63
64
65

Fig. 7.

The stoichiometric magnetite has an inverse spinel crystal structure. The tetrahedral sites (A-sites) are occupied by Fe^{3+} ions and the octahedral sites (B-sites) by the Fe^{3+} and Fe^{2+} ions. The site distribution in the MG structure is usually presented by the formula $(\text{Fe}^{3+})^A (\text{Fe}^{3+} \text{Fe}^{2+})^B \text{O}^{2-}_4$. At the temperatures above the Verwey transition temperature (~ 119 K), a rapid electron exchange exist between the Fe^{2+} and Fe^{3+} ions at the B-sites which leads to the effective $\text{Fe}^{2.5+}$ valence (Kündig and Steven Hargrove 1969, and references therein). Depending on the amount of the Fe^{2+} in the MG structure, the so called non-stoichiometric $\text{Fe}_{3-x}\text{O}_4$ or partially oxidized MG can have a range of oxidation states (Gorski and Scherer 2010; Kalska-Szostko et al. 2015). Vacancies are formed in the MG structure (presumably on the octahedral sites) to account for the charge balance. The structure of the completely oxidized MG ($x = 1/3$) is the crystal structure of the maghemite, $\gamma\text{-Fe}_2\text{O}_3$. At the room temperature (RT), only two magnetic sextets are observed in the Mössbauer spectrum of pure bulk MG (Kündig and Steven Hargrove 1969; da Costa 1995; Stevens et al. 2005; Dyar et al. 2006). The first sextet that belong to the A-site has the hyperfine magnetic field $B_{\text{hf}} \sim 49$ T and the isomer shift value characteristic for the Fe^{3+} ions $\delta \sim 0.27$ mms^{-1} . The second sextet comprises all the iron B-sites and, due to the electron hopping between iron B-sites, exhibit the hyperfine magnetic field $B_{\text{hf}} \sim 46$ T with lines broadened and shows an isomer shift of around $\delta \sim 0.67$ mms^{-1} - an averaged value of the isomer shift values for the Fe^{2+} and Fe^{3+} ions at B-sublattice. The ratio of the A to B sextets is 1:2. For the maghemite, the two sextets have very close values of the hyperfine magnetic fields, so only one sextet of $B_{\text{hf}} \sim 50$ T and isomer shift around $\delta \sim 0.32$ mms^{-1} is seen in the bulk maghemite Mössbauer spectrum at RT (Stevens et al. 2005; Dyar et al. 2006). For a partially oxidized MG or for the mixture of MG and maghemite, the relative intensities of the two sextets change, but the parameters remain essentially the same (Joos et al. 2016; Fock et al. 2017). The well-defined magnetic splitting for MG and maghemite is seen at RT only for particles with the grain size larger than 15 nm and can serve as a basis for their phase differentiation. For smaller particle grains, the magnetic splitting may collapse to a singlet or doublet due to the superparamagnetic relaxation or sextet may be severely broadened (Roggwiller and Kundig 1973; daCosta et al. 1998; Dézsi et al. 2008; Suzdalev et al. 2012; Carvalho et al. 2013; Kalska-Szostko et al. 2015; Joos et al. 2016; Oshtrakh et al. 2016). Also, in the RT-Mössbauer spectrum, superparamagnetic (SPM)-magnetite nanoparticles are hard to be distinguished from the other SPM-iron-oxide/iron-hydroxide nanoparticles (Joos et al. 2016).

Table 1. Room temperature ^{57}Fe -Mössbauer hyperfine parameters for the WL/MG and WL- γ -APS/MG samples

Sample	Mössbauer subspectrum	A (%)	Γ (mms^{-1})	$\delta / \langle \delta \rangle$ (mms^{-1})	$\Delta / \langle \Delta(\sigma) \rangle$ (mms^{-1})	$\langle B_{\text{hf}}(\sigma) \rangle$ (T)
WL/MG	D	59	0.572(8)	0.344(3)	0.827(5)	
	B-distrib.	41	0.5	0.42(9)	0	39.1(7.6)
WL- γ -APS/MG	Q-distrib.	100	0.3	0.339(5)	0.76(0.38)	

A – relative area of the Mössbauer subspectrum; Γ - line width (FWHM); δ – isomer shift; Δ - the quadrupole splitting. In the case of the distribution of the quadrupole splitting: $\langle \delta \rangle$ – average isomer shift; $\langle \Delta(\sigma) \rangle$ - average quadrupole splitting and standard deviation of the distribution of the quadrupole splitting. In case of the distribution of the magnetic splitting: $\langle \delta \rangle$ – average isomer shift; $\langle B_{\text{hf}}(\sigma) \rangle$ – average hyperfine magnetic field and standard deviation of the distribution of magnetic splitting. The fitting errors are presented in the parenthesis.

1
2
3
4 The calcium-based silicates may be also represented by the various doublets in the Mössbauer
5 spectra at RT (Dowty and Lindsley 1973; Stevens et al. 2005; Dyar et al. 2006). The doublets
6 with the isomer shift values of around 1 mms^{-1} or higher that may represent Fe^{2+} ions
7 incorporated in the calcium-silicates or silicates (Dowty and Lindsley 1973; Murad and Wagner
8 1998; Stevens et al. 2005; Dyar et al. 2006) could not be fitted to the WL- γ -APS/MG spectrum.
9 In the case of the WL/MG, the Fe^{2+} doublet originated from calcium-silicates and silicates would
10 be covered by the broadened sextet. On the other hand, the presence of the Fe^{3+} ions in silicates
11 in the two investigated samples could not be excluded, since their Mössbauer parameters are in
12 most cases overlapping with the ones of the SPM-iron-oxide/hydroxide nanoparticles (Murad
13 and Wagner 1998; Stevens et al. 2005; Dyar et al. 2006). Nevertheless, despite the difficulties
14 stated above, the most probably scenario for the two samples is that the majority of Fe is
15 incorporated in the iron-oxide nanophase. The calcium-silicate phases present in the samples
16 should exhibit an Fe^{2+} ion - Mössbauer signature as mentioned above, which could not be
17 detected in significant amount for both samples. For the WL- γ -APS/MG spectrum, the fit that
18 may distinguish between different phases in the WL- γ -APS/MG sample, *i.e.* the fit with two or
19 more doublets could not provide a unique set of Mössbauer parameters. Therefore, we decided to
20 fit the spectrum with one quadrupole splitting distribution. The average value of the quadrupole
21 splitting distribution was $\sim 0.76 \text{ mms}^{-1}$. Under assumptions that the majority of iron is
22 incorporated into the iron-oxide nanoparticles, for the WL- γ -APS/MG sample, the waste
23 majority of the ultra-fine iron-oxide nanoparticles are in the superparamagnetic state. Similar
24 reasons apply for the RT WL/MG - ^{57}Fe -Mössbauer spectrum. The dominant doublet could be
25 fitted to the WL/MG spectrum satisfactory with only one doublet and therefore may also
26 incorporate both, the SPM-iron-oxides/hydroxides and/or the silicate phases. The WL/MG -
27 ^{57}Fe -Mössbauer spectrum differs from the WL- γ -APS/MG spectrum in the presence of the
28 magnetic contribution visible as the broadened asymmetrical sextet. The fits of the magnetic part
29 of the WL/MG spectrum with the two magnetic field distributions for A- and B-site in MG phase
30 were not satisfactory. Also the fits with one discrete sextet for the A-site and one magnetic field
31 distribution for the B-site also failed to describe the spectrum reasonably. The magnetic
32 component correlated with the A-site in the MG with $B_{\text{hf}} \sim 49 \text{ T}$ was not present in the spectrum.
33 Finally, the magnetic part was fitted with one hyperfine magnetic field distribution (Fig. 7).
34 Several peaks are present in the magnetic distribution for the WL/MG sample. An attempt to fit
35 the probability distribution $P(B_{\text{hf}})$ with five Gaussian was made (Fig. 7): the most prominent
36 peak is located at $\sim 44.9 \text{ T}$ ($\delta \sim 0.36 \text{ mms}^{-1}$), followed by smaller maxima at 40.7 T ($\delta \sim$
37 0.40 mms^{-1}), 35.8 T ($\delta \sim 0.45 \text{ mms}^{-1}$), 28.5 T ($\delta \sim 0.51 \text{ mms}^{-1}$) and 21.7 T ($\delta \sim 0.58 \text{ mms}^{-1}$). The
38 peaks parameters do not indicate clearly to the specific iron-oxide/iron-hydroxide phase. Besides
39 the above mentioned reasons associated with the reducing of the particle size, there may be
40 several other reasons for the lowering of the hyperfine magnetic field at various Fe sites in the
41 iron-oxide nanoparticles and broadening of the spectrum lines: significant distribution in the
42 particles size, poorly crystallized nanoparticles, inclusion of various impurities/phases into the
43 grains, etc.

54 Scanning electron microscopy (SEM)

55
56 The SEM micrographs of the synthesized PMMA microspheres, used as a pore-forming agent,
57 and calcined unmodified and modified WL powders are shown in Fig. 8. From Fig. 8a) it can be
58 observed that the soap-free emulsion polymerization produce PMMA microspheres with high
59 uniform dimensions ($\approx 700\text{-}800 \text{ nm}$). During the calcination of the WL powder, PMMA
60
61
62
63
64
65

1
2
3
4 microspheres are subjected to degradation and evaporation which undergoes swelling and cause
5 forming of non-uniform porous structure (Fig. 8b)). Inside WL structures, noticed pores are
6 connected, as presented in Fig. 8b). Submicro-size PMMA particles, approximately 0.1-1.50
7 microns (Sreekanth Chakradhar et al. 2006; Obradović et al. 2017a), caused micro-porosity in
8 obtained material. A comparative morphology study of direct and indirect MG modified WL
9 shows that smaller MG agglomerates (Fig. 8d)) were precipitated using MG spheres attaching
10 method *via* γ -APS/DA cross-linker. Clearly visible MG agglomerates with higher dimensions
11 were obtained using the polyol-medium solvothermal method (Fig. 8c)).
12
13
14

15 These results were confirmed by EDS mapping and EDS image. The obtained results are shown
16 in Fig.9 and Table S1. The EDS image proves the presence of the starting elements O, Si, Ca and
17 Fe (Fig. 9 a) and b)). Moreover, the elemental mapping (O and Fe elements) shows clearly that
18 direct attaching of MG spheres on WL led to the precipitation of MG agglomerates of higher
19 dimensions, while attaching of MG spheres *via* γ -APS/DA cross-linker led to a more uniform
20 precipitation of MG particles of smaller dimensions. This can be attributed to numerous
21 nucleation/crystallization centers (carboxylic groups/carboxylate anions) suitable for iron
22 complexation in the initial stage, while in the course of adsorbent synthesis MG precipitation
23 take place by MG crystal growth producing a large number of more uniformly distributed
24 smaller particle size on WL/DA surface (Fig.1). Numerous crystallization centers affect the MG
25 loading. Hence, as shown in the results of the EDS analysis (Table S1), a higher loading of MG
26 was bounded by precipitation *via* γ -APS/DA cross-linker (11.36%), while only 4.37% were
27 bounded by direct MG precipitation. These results were corroborated by acidic dissolution in
28 nitric acid and determination of iron content (10.66% for WL/ γ -APS/DA and 4.76% for
29 WL/MG).
30
31
32
33

34 **Fig. 8.**

35 **Fig.9.**

36 **Determination of the point of zero charge (pH_{PZC}) of wollastonite-based** 37 **adsorbent and effect of pH on adsorption efficiency**

38
39 The pH influences the state of equilibrium of ionic species and protonation/deprotonation of
40 sorbent functional groups. The pH of the point of zero charge, pH_{PZC} for the magnetite modified
41 WL based adsorbents was measured by the pH drift method. In aqueous systems, the surface of
42 iron oxides is covered with FeOH groups that can be protonated or deprotonated and generate
43 surface charge $FeOH_2^+$ or FeO^- at pH values below or above the point of zero charge for
44 magnetite (pH_{PZC}), respectively(Rajput et al. 2016). Electrostatic forces between metal ion
45 species and surface charges are responsible for adsorption (Ahmed et al. 2013; Rajput et al.
46 2016). The point of zero charge for magnetite is the pH value at which the surface concentrations
47 of $FeOH^{2+}$ and FeO^- groups are equal. The measured pH_{PZC} of unmodified WL was 2.7, while
48 pH_{PZC} of both MG modified WL based adsorbents was ~ 7.0 . In the next step, the removal degree
49 of Ni^{2+} and Cd^{2+} *versus* the initial pH (pH_i) was studied, and the obtained results are presented in
50 Fig.S1. At low pH (lower than pH_{PZC} of MG modified WL), sorbent surface is covered mostly
51 with $FeOH^{2+}$ and positively charged surface functionalities. Therefore, the positively charged
52 metal ions, Ni^{2+} and Cd^{2+} , showed low adsorption efficiency due to both the repulsive forces and
53 the adsorption of H_3O^+ which hinders/competitively occupy adsorptive sites (Ahmed et al. 2013).
54
55
56
57
58
59
60
61
62
63
64
65

1
2
3
4 It can be noticed from Fig.S1 that, with an increase in pH from 3 to 9, the Cd²⁺ and Ni²⁺
5 percentage uptake increased too. In the pH range between 7 and 9 the maximum of Ni²⁺ and Cd²⁺
6 percentages uptake was observed (72 % and 97 % Cd²⁺ uptake on WL/MG and WL-γ-APS/MG,
7 receptively, and 84 % and 85 % Ni²⁺ uptake on WL/MG and WL-γ-APS/MG, receptively).
8 Subsequently gradual decrease of Cd²⁺ and Ni²⁺ uptake on was WL/MG and WL-γ-APS/MG
9 observed at pH>8. The variation in the effectiveness of metal removal at different pH values
10 could be explained by metal speciation as shown in Fig. S2. From the speciation diagram of Cd²⁺
11 and Ni²⁺ ion (Fig.S2), obtained by using MINTEQ. 3.0 software (Gustafsson 2011), high
12 removal efficiencies would be expected in the pH region 7-8 for both Cd²⁺ and Ni²⁺, while
13 adsorption capabilities at pH>8 could originate from additional contribution of the precipitation
14 of insoluble metal hydroxides (Drah et al. 2017). Thus adsorption curves for studied cations
15 represent only adsorption with excluded precipitation at pH>8. According to this, at pH<8, it was
16 certain that removals of Cd²⁺ and Ni²⁺ were not affected by hydroxide/salt precipitation, and
17 obtained results were considered without any misleading conclusions (Drah et al. 2017). In this
18 sense, the selection of pH 7.5 for Cd²⁺ and Ni²⁺ removal and pH 6.5 for both Cr(VI), considering
19 equilibrium of HCrO₄⁻/CrO₄²⁻ ions, and phosphate, equilibrium of H₂PO₄⁻/HPO₄²⁻ ions, was an
20 adequate choice to achieve high adsorption capacities.
21
22
23
24
25
26

27 **Adsorption/desorption study of Cd²⁺, Ni²⁺, HCrO₄⁻/CrO₄²⁻ and H₂PO₄⁻/HPO₄²⁻** 28 **on WL/MG and WL-γ-APS/MG adsorbents** 29

30 According to the previous adsorptions studies, it was confirmed that heavy metals undergo
31 complexation and hydrolysis during adsorption (Kumari et al. 2015). Surface complexation of
32 heavy metals occurs *via* exchange of metal ions M^{m+} with H⁺ ions at the surface hydroxyl groups
33 -M'OH. M(OH)_n^{(m-n)+} ions, that occurs during the hydrolysis, can electrostatically interact with
34 the iron-oxide (MG) surfaces forming a specific type of adsorbed ion/surface interaction (Petrova
35 et al. 2011). It was found that metals hydrolysis causes weakening of the interaction between the
36 metal ion and water in hydration shell that facilitates the approach of the metal ions to the
37 surface (Petrova et al. 2011).
38
39

40 However, analysis/description of adsorption mechanism of oxyanions is complex/extensive task
41 and needs more reliable results, and most of them are based on spectroscopic evidence (Kumari
42 et al. 2015). Multiple adsorption mechanisms occur during the phosphate ions up-taking. The
43 cationic species (M(OH)_n^{(m-n)+}) takes part in uptaking of phosphate ions via electrostatic
44 interaction (Rout et al. 2015, 2016). However, it is proved that complexation of oxyanions on
45 MG surface was achieved by formation of monodentate and bidentate complexes through
46 covalent bonding between the surface oxide's oxygen and the adsorbing metal ion (Kumari et al.
47 2015). Three main forms of phosphate complexes on iron oxide surface were defined: protonated
48 ((FeO)₂(OH)PO), nonprotonated bridging bidentate ((FeO)₂PO₂) and a nonprotonated
49 monodentate ((FeO)PO₃) (Tejedor-Tejedor and Anderson 1990). In a similar manner due to
50 similar chemistry chromate, schematic illustration of formation of monodentate and bidentate
51 complexes between MG modified WL and HCrO₄⁻/CrO₄²⁻ ions is presented on Fig. S3.
52
53
54
55

56 The state of interaction/bonding at solutes/sorbent surface can be described by fitting
57 experimental data with various adsorption isotherms (Markovski et al. 2014b). Analysis of
58 adsorption data was performed by using various isotherm models, and statistical criteria used to
59 evaluate the quality of model fitting of adsorption data. The Langmuir isotherm model is given
60
61
62
63
64
65

1
2
3
4 by Eq. (2), while thermodynamic parameters for studied ions were first estimated using the
5 Gibbs free energy equation and the linearized van't Hoff Equation (*i.e.*, the van't Hoff plot) as
6 follows (Liu et al. 2015):
7

$$q_e = (Kq_{\max}C_e)/(1 + KC_e) \quad (2)$$

$$\Delta G^o = -RT\ln K_L \quad (3)$$

$$\ln K_L = -\frac{\Delta H^o}{RT} + \frac{\Delta S^o}{R} \quad (4)$$

16 where: C_e is the equilibrium concentration of ion at equilibrium (mol l^{-1}), q_e is the amount of ions
17 adsorbed per weight unit of solid at equilibrium (mol g^{-1}), K and K_L are Langmuir constants
18 related to sorption affinity in l mg^{-1} and l mol^{-1} , respectively, and q_{\max} is maximum sorption
19 capacity (mol g^{-1}), ΔG^o (kJ mol^{-1}) is the change of free energy, ΔH^o (kJ mol^{-1}) is the change of
20 enthalpy, ΔS^o (kJ mol^{-1}) is the change of entropy, T (K) is the absolute temperature and R is the
21 ideal gas constant ($0.008314 \text{ kJ mol}^{-1} \text{ K}^{-1}$). The values of non-linear Langmuir adsorption
22 isotherm and thermodynamic parameters at 298, 308 and 318 K for Cd^{2+} , Ni^{2+} , $\text{HCrO}_4^-/\text{CrO}_4^{2-}$
23 and $\text{H}_2\text{PO}_4^-/\text{HPO}_4^{2-}$ ions adsorption, using WL/MG and WL- γ -APS/MG adsorbents, are presented
24 in Tables 2 and 3, and Fig. S4. Linear Langmuir adsorption isotherms, as well as values of the q_e ,
25 K and K_L are presented in Fig. S5, and Tables S2 and S3.
26
27
28

29 According to the Langmuir isotherm, mechanism of Cd^{2+} , Ni^{2+} , $\text{HCrO}_4^-/\text{CrO}_4^{2-}$ and phosphate
30 ions adsorption onto WL/MG and WL- γ -APS/MG sorbents can be described by monolayer
31 adsorption with equal energy and enthalpy for all adsorption sites. Langmuir isotherm assumed
32 that the energy of adsorption is generally considerably larger than for the second and higher
33 layers, and therefore multilayer formation is less possible (Rouquerol et al. 1999).
34
35

36 The results presented in Table 2 show high predicted adsorption capacity for both WL/MG and
37 WL- γ -APS/MG adsorbents, and increase of adsorption capacity with the temperature increase.
38 Moreover, adsorption results significantly support better adsorption performances of WL- γ -
39 APS/MG (26.7 – 33.0 % higher q_e) due to developed surface formed by size- and distribution
40 controllable deposition of MG on WL/DA.
41
42

43 The higher values of the Langmuir constant, that reflect the sorption affinity, were obtained for
44 adsorption of all ions on WL- γ -APS/MG adsorbents at all temperatures. Higher temperature
45 dependence was obtained for $\text{H}_2\text{PO}_4^-/\text{HPO}_4^{2-}$ and $\text{HCrO}_4^-/\text{CrO}_4^{2-}$ oxyanions, which means higher
46 probability of surface complexation at higher temperature. Comparing obtained values of the
47 Langmuir constant it can be concluded that WL/MG and WL- γ -APS/MG adsorbents have higher
48 sorption affinity for Ni^{2+} and Cd^{2+} as a results of their bonding mechanism. It can be explained by
49 complex formation of monodentate mononuclear and bidentate binuclear complexes of HCrO_4^-
50 $/\text{CrO}_4^{2-}$ and $\text{H}_2\text{PO}_4^-/\text{HPO}_4^{2-}$ ions with MG surface hydroxylic groups, while Ni^{2+} and Cd^{2+} ions
51 easily create electrostatic interactions with MG centers. Moreover, the complexation of all
52 investigated pollutant is easier with developed surface of W- γ -APS/MG adsorbent.
53
54
55
56
57
58
59
60
61
62
63
64
65

Table 2. Non-linear Langmuir isotherm parameters for Cd^{2+} , Ni^{2+} , $\text{H}_2\text{PO}_4^-/\text{HPO}_4^{2-}$ and $\text{HCrO}_4^-/\text{CrO}_4^{2-}$ ions obtained at 298, 308 and 318 K using WL/MG and WL- γ -APS/MG adsorbents

	Cd^{2+}				Ni^{2+}		
	$T(\text{K})$	q_e (mg g^{-1})	K (l mg^{-1})	R^2	q_e (mg g^{-1})	K (l mg^{-1})	R^2
WL/MG	298	50.543	24.313	0.960	47.889	23.330	0.936
	308	53.429	22.389	0.922	50.216	22.856	0.909
	318	55.450	25.867	0.969	52.019	26.911	0.969
WL-γ-APS/MG	298	69.289	19.096	0.876	61.412	24.638	0.989
	308	69.724	44.152	0.986	63.076	28.920	0.979
	318	73.126	61.886	0.986	66.144	37.083	0.988
	$\text{H}_2\text{PO}_4^-/\text{HPO}_4^{2-}$				$\text{HCrO}_4^-/\text{CrO}_4^{2-}$		
	T (K)	q_e (mg g^{-1})	K (l mg^{-1})	R^2	q_e (mg g^{-1})	K (l mg^{-1})	R^2
WL/MG	298	44.529	17.021	0.943	42.824	14.940	0.844
	308	46.262	19.060	0.947	44.447	13.262	0.808
	318	48.132	19.637	0.962	47.382	14.477	0.829
WL-γ-APS/MG	298	60.019	35.202	0.957	62.133	12.071	0.903
	308	62.702	35.921	0.981	63.632	19.354	0.917
	318	64.168	38.153	0.965	63.456	37.923	0.973

Table 3. Thermodynamic parameters Cd^{2+} , Ni^{2+} , $\text{H}_2\text{PO}_4^-/\text{HPO}_4^{2-}$ and $\text{HCrO}_4^-/\text{CrO}_4^{2-}$ ions obtained at 298, 308 and 318 K using WL/MG and WL- γ -APS/MG adsorbents

	Cd^{2+}				Ni^{2+}		
	T (K)	ΔG° (kJ mol^{-1})	ΔH° (kJ mol^{-1})	ΔS° ($\text{J mol}^{-1} \text{K}^{-1}$)	ΔG° (kJ mol^{-1})	ΔH° (kJ mol^{-1})	ΔS° ($\text{J mol}^{-1} \text{K}^{-1}$)
WL/MG	298	-45.23	2.15	159.10	-45.20	2.01	158.75
	308	-47.01			-47.01		
	318	-48.40			-48.36		
WL-γ-APS/MG	298	-46.21	12.64	198.04	-45.19	9.32	183.33
	308	-48.80			-47.48		
	318	-50.14			-48.83		
	$\text{H}_2\text{PO}_4^-/\text{HPO}_4^{2-}$				$\text{HCrO}_4^-/\text{CrO}_4^{2-}$		
	T (K)	ΔG° (kJ mol^{-1})	ΔH° (kJ mol^{-1})	ΔS° ($\text{J mol}^{-1} \text{K}^{-1}$)	ΔG° (kJ mol^{-1})	ΔH° (kJ mol^{-1})	ΔS° ($\text{J mol}^{-1} \text{K}^{-1}$)
WL/MG	298	-39.61	8.69	161.88	-41.34	5.36	156.65
	308	-41.11			-42.92		
	318	-42.86			-44.48		
WL-γ-APS/MG	298	-40.09	29.10	231.46	-40.69	21.50	208.95
	308	-41.89			-43.13		
	318	-44.79			-44.85		

The negative ΔG° values indicate that adsorption occurs via spontaneous reactions (Veličković et al. 2012). Structure and stability of multilayered hydrated ions, charged or neutral, depend on pH and temperature. Changes in pH value dictate presence of ionic species which in turn affect structure/extent of interaction in hydration shell. Desolvation and diffusion at higher

1
2
3
4 temperatures are more feasible processes, which are noticed as slight ΔG° increase with
5 temperature increase. According to general rules, the change of ΔG° for physisorption lies
6 between -20 and 0 kJ mol⁻¹, both physisorption and chemisorption in the range from -20 to -
7 80 kJ mol⁻¹, while the chemisorption between -80 and -200 kJ mol⁻¹. Obtained results indicate
8 contribution of both physisorption and chemisorption (Vuković et al. 2010, 2011; Budimirović et
9 al. 2017).

10
11
12 The positive ΔH° also indicates the endothermic nature of adsorption for all studied ions(Liu et
13 al. 2015) (Table 3). The ΔH° does not significantly vary between cations adsorption on WL/MG,
14 while slightly increases for Cd²⁺ adsorption on WL- γ -APS/MG. The highest ΔH° values are
15 obtained for WL- γ -APS/MG for oxyanions. Low endothermic nature reflect low energy
16 released/consumed by desolvation of cation and formation of an M²⁺/surface interactions, which
17 could at appropriate balance. Higher ΔH° for oxyanions adsorption indicates higher energetic
18 contribution of surface reaction, and diffusional processes at lower extent. All of these
19 contributing elementary processes are individually low to significant, and could be either
20 exothermic or endothermic, and their summary effect was found to be low endothermic.
21
22
23

24 The positive ΔS° relates to desolvation of structurally ordered hydronium ion and subsequent
25 increase in randomness with increased concentration of adsorbed ions on the solid surface(Liu et
26 al. 2015). Water molecules in surrounding solvation shell of metal ion form ordered structure,
27 which after disruption of hydrogen-bonding increase system disorder. Positive values of entropy
28 change (ΔS°) indicate the increase in disorder (randomness) on boundary solid-liquid surface.
29 The M²⁺/surface interactions and oxyanions complexes formation means decrease in
30 translational, rotational and vibrational motion which contributes to entropy decrease.
31 Simultaneously, ΔS° increases due to both liberation of water due to adsorption and from cation
32 hydration shell.
33
34
35

36 Except for this, results of reusability study showed low decrease of adsorption efficiency after three
37 adsorptions/desorption cycles. An adsorption efficiency decrease of 22 %, 20 %, 25 % and 18 %
38 for Cd²⁺, Ni²⁺, HCrO₄⁻/CrO₄²⁻ and H₂PO₄⁻/HPO₄²⁻ ions, respectively, was obtained after the third
39 adsorption/desorption cycle using WL/MG adsorbent. Hence, lower decrease of adsorption
40 efficiency of 18 %, 17 %, 19 % and 13 % for Cd²⁺, Ni²⁺, HCrO₄⁻/CrO₄²⁻ and H₂PO₄⁻/HPO₄²⁻ ions,
41 respectively, was obtained after the third adsorption/desorption cycle using WL- γ -APS/MG
42 adsorbent. According to this, it can be concluded that modification of WL based ceramic (support)
43 with magnetic iron-oxide form (magnetite) *via* γ -APS/DA cross-linker gave adsorbent with higher
44 stability of MG deposit. Moreover, with proper selection of technology for treatment of spent
45 waste alkali concentrated Cd²⁺, Ni²⁺, HCrO₄⁻/CrO₄²⁻ and H₂PO₄⁻/HPO₄²⁻ ions provide safe
46 technology for their removal.
47
48
49

50 **Competitive adsorption study of Cd²⁺, Ni²⁺, HCrO₄⁻/CrO₄²⁻ and H₂PO₄⁻/HPO₄²⁻** 51 **ions removal from real water sample** 52

53
54 Evaluation of WL/MG and WL- γ -APS/MG adsorbents potential use for Cd²⁺, Ni²⁺, HCrO₄⁻
55 /CrO₄²⁻ and H₂PO₄⁻/HPO₄²⁻ ions removal from real water samples, contaminated natural water
56 from the area of the city of Zrenjanin (located in Vojvodina, Serbia), was used for sorption
57 experiment before any purification treatment. Other anions of interest presents in water sample
58 are SO₄²⁻ (42.5ppm) and Cl⁻ (1.2 ppm) (Taleb et al. 2016b). Kinetic experiments performed with
59
60
61
62
63
64
65

1
2
3
4 100 ppm of WL/MG and WL- γ -APS/MG adsorbents were carried out to find out the level of the
5 efficiency of total Cd²⁺, Ni²⁺, HCrO₄⁻/CrO₄²⁻ and H₂PO₄⁻/HPO₄²⁻ ions removal in natural water
6 sample. It was found that competition of SO₄²⁻ and Cl⁻ ions was negligible (Petrova et al. 2011).
7
8

9 **Adsorption kinetic study**

10
11 Effect of time on pollutant adsorption was studied in a batch system containing m/V 125 mg l⁻¹
12 of adsorbent at pH of 6.5±0.10 for Cd²⁺ and Ni²⁺ and of 7.5±0.10 for HCrO₄⁻/CrO₄²⁻ and H₂PO₄⁻
13 /HPO₄²⁻ ions. The ions concentration was determined after 5, 10, 15, 30, 60, and 90 min. In order
14 to properly describe adsorption kinetic, the obtained experimental data was fitted using different
15 kinetic rate equations (Bizerea Spiridon and Pitulice 2014). According to the highest values of
16 correlation coefficient, R^2 , which is a measure of conformity between experimental data and
17 calculated ones, it was proved that pseudo-second-order (PSO), *i.e.* Eq. (5), was the most
18 appropriate model for description of kinetic processes for both WL/MG and WL- γ -APS/MG
19 adsorbents (Tables 4 and S4, Fig. S6 (linear) and S7 (non-linear fit)):
20
21

$$22 \frac{dq_t}{dt} = k_2(q_e - q_t)^2 \quad (5)$$

23
24
25 The adsorption capacities at equilibrium and at time t (min) are defined by q_e and q_t (mg g⁻¹)
26 respectively, k_2 is the PSO rate constant (g mg⁻¹ min⁻¹). The kinetic parameters, presented in
27 Table 4, showed that both sorbents, and preferentially WL- γ -APS/MG, possess high affinity with
28 respect to studied ions, and satisfactory rate at which system attain its equilibrium. According to
29 pseudo second-order kinetic law, the rate limiting step may be chemical adsorption involving
30 valent forces through sharing or the exchange of electrons between the sorbents and divalent
31 metal ions (Qiu et al. 2009). The analysis of kinetic data, using PSO kinetic method, resulted in
32 significantly higher rate constant (1.17 to 13.4 times higher) and relatively balanced values of
33 adsorption capacity of studied ions using WL- γ -APS/MG adsorbent at all temperatures. The k_2
34 values increase with the increasing the temperature and the highest values are obtained at 318 K.
35 These results indicate more efficient diffusional transport/adsorbate complexation at adsorbent
36 surface *versus* temperature increase. Determination of activation parameters could give
37 information on both energetic requirements to overcome slowest adsorption step and adsorption
38 mechanism. The energy of activation (E_a) was calculated from the linear plot of the values of
39 logarithms of rate constants (k_2) *versus* $1/T$ obtained by linearization of Arrhenius equation (Eq.
40 6) (results obtained in kinetic study at 298 K using the Eq. (5) (March 1985):
41
42
43
44

$$45 k_2 = Ae^{-(E_a/RT)} \quad (6)$$

46
47
48 Adsorption kinetics is generally controlled by diffusive mass transfer, thus rates of approaching
49 to equilibrium usually increase with increasing of temperature. For the cations adsorption on
50 both adsorbents, the results show that the intra-particle diffusion is a rate-controlling step since
51 the activation energy is low and within the range of 6–17.5 kJ mol⁻¹ characteristic for diffusion-
52 controlled processes (Haring 1942). The higher activation energies for the adsorption of
53 oxyanions reflect significance of morphological/porosity factor to improved adsorption kinetic.
54
55
56
57
58
59
60
61
62
63
64
65

Table 4. Kinetic and activation parameters obtained by the use of non-linear PSO kinetic model for the Cd²⁺, Ni²⁺, HCrO₄⁻/CrO₄²⁻ and H₂PO₄⁻/HPO₄²⁻ removal using WL/MG and WL-γ-APS/MG adsorbents

298 K			
	Pseudo-second order	Cd ²⁺	Ni ²⁺
WL/MG	k ₂ x10 ² (g mg ⁻¹ min ⁻¹)	0.193±0.029	0.208±0.009
	q _e (mg g ⁻¹)	55.878±1.003	54.618±1.125
	R ²	0.960	0.973
	Ea (kJ mol ⁻¹)	11.43	17.38
WL-γ-APS/MG	k ₂ x10 ² (g mg ⁻¹ min ⁻¹)	1.222±0.021	1.187±0.005
	q _e (mg g ⁻¹)	70.027±1.112	62.563±1.082
	R ²	0.992	0.991
	Ea (kJ mol ⁻¹)	20.78	24.20
298 K			
	Pseudo-second order	H ₂ PO ₄ ⁻ /HPO ₄ ²⁻	HCrO ₄ ⁻ /CrO ₄ ²⁻
WL/MG	k ₂ x10 ² (g mg ⁻¹ min ⁻¹)	0.594±0.012	0.248±0.017
	q _e (mg g ⁻¹)	42.819±1.124	46.982±1.115
	R ²	0.927	0.972
	Ea (kJ mol ⁻¹)	13.91	27.12
WL-γ-APS/MG	k ₂ x10 ² (g mg ⁻¹ min ⁻¹)	1.018±0.010	1.215±0.020
	q _e (mg g ⁻¹)	60.638±0.719	59.574±1.108
	R ²	0.947	0.952
	Ea (kJ mol ⁻¹)	28.92	25.02
308 K			
	Pseudo-second order	Cd ²⁺	Ni ²⁺
WL/MG	k ₂ x10 ² (g mg ⁻¹ min ⁻¹)	0.223±0.012	0.238±0.001
	q _e (mg g ⁻¹)	59.445±0.748	58.931±1.197
	R ²	0.988	0.975
WL-γ-APS/MG	k ₂ x10 ² (g mg ⁻¹ min ⁻¹)	2.075±0.007	2.030±0.007
	q _e (mg g ⁻¹)	69.883±1.221	62.411±1.223
	R ²	0.999	0.998
308 K			
	Pseudo-second order	H ₂ PO ₄ ⁻ /HPO ₄ ²⁻	HCrO ₄ ⁻ /CrO ₄ ²⁻
WL/MG	k ₂ x10 ² (g mg ⁻¹ min ⁻¹)	0.785±0.003	0.282±0.001
	q _e (mg g ⁻¹)	45.300±1.022	47.734±1.690
	R ²	0.994	0.995
WL-γ-APS/MG	k ₂ x10 ² (g mg ⁻¹ min ⁻¹)	2.452±0.008	2.402±0.003
	q _e (mg g ⁻¹)	61.336±1.103	62.494±0.426
	R ²	0.973	0.947
318 K			
	Pseudo-second order	Cd ²⁺	Ni ²⁺
WL/MG	k ₂ x10 ² (g mg ⁻¹ min ⁻¹)	0.258±0.007	0.324±0.001
	q _e (mg g ⁻¹)	54.621±2.686	55.410±1.303
	R ²	0.997	0.986
WL-γ-APS/MG	k ₂ x10 ² (g mg ⁻¹ min ⁻¹)	2.068±0.002	2.183±0.008
	q _e (mg g ⁻¹)	73.092±0.299	65.730±0.987
	R ²	0.992	0.979
318 K			
	Pseudo-second order	H ₂ PO ₄ ⁻ /HPO ₄ ²⁻	HCrO ₄ ⁻ /CrO ₄ ²⁻
WL/MG	k ₂ x10 ² (g mg ⁻¹ min ⁻¹)	0.851±0.004	0.496±0.001
	q _e (mg g ⁻¹)	46.939±1.001	47.402±1.112
	R ²	0.966	0.939
WL-γ-APS/MG	k ₂ x10 ² (g mg ⁻¹ min ⁻¹)	2.097±0.004	2.332±0.004
	q _e (mg g ⁻¹)	63.999±0.682	63.184±0.636
	R ²	0.899	0.993

The kinetic data results (Table S5) obtained by applying Weber–Morris (W-M) kinetic model were useful in evaluation of rate limiting step of overall process (Vuković et al. 2011). High values of W-M constant C_1 for both cations and oxyanions (Table S5) indicate that intra-particle diffusion is not the only rate-limiting step; complex influence of the other factors determine effectiveness of overall pollutant transport. At the initial stage of the process, the diffusion from bulk phase to the exterior surface takes place at high rate, while second linear part, which depends on material porosity, relate to the diffusion inside mesopores/micropores.

Various adsorbents for Cd^{2+} , Ni^{2+} , $\text{HCrO}_4^-/\text{CrO}_4^{2-}$ and $\text{H}_2\text{PO}_4^-/\text{HPO}_4^{2-}$ ions removal, including unmodified and iron-oxide modified materials such as activated carbon, clays, cellulose based materials and WL based sorbents were reported in literature (Vuković et al. 2010; Karnib et al. 2014; Taleb et al. 2016b). Cd^{2+} , Ni^{2+} , $\text{HCrO}_4^-/\text{CrO}_4^{2-}$ and $\text{H}_2\text{PO}_4^-/\text{HPO}_4^{2-}$ ions adsorption capacities (value of q_e derived from Langmuir equation) of various WL and magnetite based adsorbents are summarized in Table S6. According to the presented Cd^{2+} , Ni^{2+} , $\text{HCrO}_4^-/\text{CrO}_4^{2-}$ and $\text{H}_2\text{PO}_4^-/\text{HPO}_4^{2-}$ ions adsorption capacities on WL and MG based adsorbents, with regard to other equilibrium contact times, the applied adsorbent in the present study could potentially be used as efficient adsorbent to remove Cd^{2+} , Ni^{2+} , $\text{HCrO}_4^-/\text{CrO}_4^{2-}$ and $\text{H}_2\text{PO}_4^-/\text{HPO}_4^{2-}$ ions from aqueous solutions in a short time period. Both, bare WL and MG nanoparticles showed moderate adsorption capacities ($6.5 - 13.5 \text{ mg g}^{-1}$) for Cd^{2+} , Ni^{2+} , $\text{HCrO}_4^-/\text{CrO}_4^{2-}$ and $\text{H}_2\text{PO}_4^-/\text{HPO}_4^{2-}$ ions removal. Moreover, hybrid adsorbents obtained by MG precipitation on porous WL support showed higher adsorption capacities ($52.41 - 73.15 \text{ mg g}^{-1}$) due to availability of more active sites for heavy metals removal and oxyions complexation.

Monolayer model for single-compound adsorption

For the monolayer model for single-compound adsorption it is assumed that heavy metal ions/oxyanions are adsorbed with one energy ($-\varepsilon$) (Sellaoui et al. 2017a). The $-\varepsilon$ describes the interaction of ions with the surface of the MG-modified WL-based sorbents. **Adsorption energy is calculated according to the following equation (Sellaoui et al. 2017b):**

$$\varepsilon = k_B T \ln \left(\frac{c_s}{c_{1/2}} \right) \quad (7)$$

where k_B Boltzmann constant, c_s is the solubility of the heavy metal and $c_{1/2}$ is the concentration at half saturation (Sellaoui et al. 2016b, a). According to the general Langmuir model interpretation, each adsorption site accommodates one ion, as following chemical pseudo-reactions describe (Sellaoui et al. 2017b, a):



where A^{2+} represents the adsorbed Cd^{2+} or Ni^{2+} ions, S is the adsorbent receptor site, $\text{A}^{2+}n\text{S}$ represents formed complex of cations with MG-modified WL-based sorbents, n represents number of the bonded ions per one receptor site, B^- and B^{2-} represent the mono- and divalent chromate or phosphate oxyanions, and B^-nS and $\text{B}^{2-}n\text{S}$ represent formed complexes of oxyanions

with MG-modified WL-based sorbents. The partition function of one identical site and the monolayer model for single-compound adsorption are described by following equations:

$$Z_{gc} = 1 + e^{\beta(\varepsilon+\mu)} \quad (11)$$

$$Z_{gc} = e^{\beta(\varepsilon+\mu)N_M} \quad (12)$$

$$Q = \frac{nN_M}{1 + \left(\frac{c_{1/2}}{c}\right)^n} \quad (13)$$

In these expressions, ε represents the adsorption energy of the receptor site, μ is the chemical potential of the adsorbed state determined from the Gibbs free energy, β is the Boltzmann factor, defined as $1/(k_B T)$, Q is the adsorption capacity, n is the number of ions per site, N_M is the density of receptor site, and c is the heavy metal ion/oxyanion equilibrium concentration (Sellaoui et al. 2016b, a). Different values for the parameters for single-compound adsorption of heavy metal ions/oxyanions on MG-modified WL-based sorbents are presented in Table 5.

Table 5. Values of adjustable parameters in single-compound system for adsorption of Cd^{2+} , Ni^{2+} , $\text{HCrO}_4^-/\text{CrO}_4^{2-}$ and $\text{H}_2\text{PO}_4^-/\text{HPO}_4^{2-}$ ions

	Cd^{2+}					Ni^{2+}			
	T (K)	ε , (KJ mol ⁻¹)	Q_{sat} (mg g ⁻¹)	N_M (mg g ⁻¹)	n	ε , (KJ mol ⁻¹)	Q_{sat} (mg g ⁻¹)	N_M (mg g ⁻¹)	n
WL/MG	298	7.624	55.878	45	0.66	6.781	54.618	44	1.21
	308	7.967	59.445	45	0.85	7.108	58.931	44	0.91
	318	7.388	54.621	45	1.11	7.411	55.410	44	0.88
WL- γ - APS/MG	298	7.698	70.027	45	0.82	6.822	62.563	44	0.70
	308	8.024	69.883	43	0.96	7.126	62.411	43	0.99
	318	8.491	73.092	43	1.21	8.388	65.730	44	1.25
	$\text{HCrO}_4^-/\text{CrO}_4^{2-}$					$\text{H}_2\text{PO}_4^-/\text{HPO}_4^{2-}$			
	T (K)	ε , (KJ mol ⁻¹)	Q_{sat} (mg g ⁻¹)	N_M (mg g ⁻¹)	n	ε , (KJ mol ⁻¹)	Q_{sat} (mg g ⁻¹)	N_M (mg g ⁻¹)	n
WL/MG	298	6.310	46.982	49	0.65	6.059	42.819	53	0.58
	308	6.715	47.734	49	0.66	6.364	45.300	53	0.59
	318	7.097	47.402	49	0.73	8.649	46.939	52	0.59
WL- γ - APS/MG	298	6.397	59.574	50	0.57	6.181	60.638	52	0.67
	308	6.364	62.494	48	0.57	6.479	61.336	55	0.68
	318	6.650	63.184	48	0.59	6.779	63.999	50	0.69

The determination of the number of ions that interact with one receptor site offers reliable information complementing the conclusions for adsorption phenomena obtained from the isothermal adsorption study. If the number of the bonded/complexed ions/oxyanions per site is lower than 1, the ions interact with at least two receptor sites (multi-link). Opposite, if the n is higher than 1, the receptor site is occupied minimum by one ion (Sellaoui et al. 2017b, a). For all of the investigated single-compound systems (adsorption of Cd^{2+} , Ni^{2+} , $\text{HCrO}_4^-/\text{CrO}_4^{2-}$ and $\text{H}_2\text{PO}_4^-/\text{HPO}_4^{2-}$ on WL based adsorbents), the lowest values of the n are obtained at 298 K. It confirms that the main mechanism of the Cd^{2+} and Ni^{2+} ions adsorption occurs via exchange of metal ions $\text{Cd}^{2+}/\text{Ni}^{2+}$ with H^+ ions at the surface hydroxyl groups $-\text{FeOH}$ (receptor site)

1
2
3
4 producing $\text{Cd}^{2+}/\text{Ni}^{2+}(\text{OH})^+$ ions that are bonded with another MG modified WL receptor site.
5 Also, electrostatic interactions of ion positive charge with electron pair of hydroxyl groups could
6 be of appropriate significance. By changing the adsorption operational conditions (increasing
7 temperature) the values of the n increase as well. For the Cd^{2+} ions adsorption on both WL-MG
8 and WL- γ -APS/MG adsorbents the highest values of n (higher than 1) are obtained at 318 K.
9 This indicates appropriate change of metal binding mechanism, *i.e.* higher number of ions per
10 one site, with concomitant increase of adsorption capacity (Table 2). Opposite is found for Ni^{2+}
11 ions adsorption on WL-MG adsorbent where the highest values of n is obtained at 298 K. Lower
12 values of n parameters are found for the $\text{HCrO}_4^-/\text{CrO}_4^{2-}$ and $\text{H}_2\text{PO}_4^-/\text{HPO}_4^{2-}$ ions (Table 5)
13 indicating different adsorption mechanism in relation to cations. The n values in the range 0.57-
14 0.73 for $\text{HCrO}_4^-/\text{CrO}_4^{2-}$ and 0.59-0.69 for $\text{H}_2\text{PO}_4^-/\text{HPO}_4^{2-}$ indicates that main mechanism
15 represent interaction one ion per two active surface sites which is in good accordance with
16 creation of bidentate mononuclear and binuclear surface complexes of both ions (Zach-Maor et
17 al. 2011; Johnston and Chrysochoou 2014). The parameter n also increases with temperature
18 increase.

23 Conclusion

24
25
26
27 Magnetite modified porous wollastonite-based ceramics were synthesized using ultra-fine
28 PMMA as a pore-forming agent in order to obtain hybrid adsorbents with high adsorption
29 performances for heavy metals and oxyanions. FTIR, Raman, XRD and Mössbauer
30 measurements confirmed wollastonite and larnite phases at pure WL support and successfulness
31 of magnetite precipitation. SEM analysis confirmed macro and micro porosity of pure WL
32 support and formation of MG aggregates on WL. Synthesized MG-modified WL-based sorbent
33 was used for Cd^{2+} , Ni^{2+} , $\text{HCrO}_4^-/\text{CrO}_4^{2-}$ and $\text{H}_2\text{PO}_4^-/\text{HPO}_4^{2-}$ ions removal. Results showed that
34 pH is an important parameter that controls the effectiveness of pollutant removal.

35
36
37 The quality of the isotherm modeling of adsorption data was estimated by the correlation
38 coefficients. The best adsorption model was found to be the Langmuir isotherm. The kinetic data
39 of the sorption were well fitted with the pseudo-second-order kinetic model. A significantly
40 higher second-order rate constant of Cd^{2+} , Ni^{2+} , $\text{HCrO}_4^-/\text{CrO}_4^{2-}$ and $\text{H}_2\text{PO}_4^-/\text{HPO}_4^{2-}$ ions
41 adsorption was obtained using WL- γ -APS/MG as adsorbent. Higher activation energies were
42 obtained for oxyanion adsorption.

43
44
45 Statistical physic theory was used for interpretation of single adsorption isotherms and
46 adsorption phenomena. The absorption parameters in a single-compound system deduced by the
47 monolayer model with one energy confirmed that the adsorption of Cd^{2+} and Ni^{2+} ions occurred
48 via mostly one ion with two receptor sites interactions. For the $\text{HCrO}_4^-/\text{CrO}_4^{2-}$ and H_2PO_4^-
49 $/\text{HPO}_4^{2-}$ ions adsorption, the statistical physic model confirmed that multiple adsorption
50 mechanisms electrostatic interaction/complexation occurred.
51
52
53
54
55
56
57
58
59
60
61
62
63
64
65

Acknowledgement

This research was performed within the projects OI 172057, OI 171001, and 176018, funded by the Ministry of Education, Science and Technological Development of the Republic of Serbia, and bilateral cooperation between Serbia and France, No. 4510339/2016/09/03 “Intelligent eco-nanomaterials and nanocomposites”. The work was supported in part by the National Science Foundation, North Carolina State University (Project No. HRD-1345219 and DMR-1523617) and the National Aeronautics and Space Administration project (NASA: NNX09AV07A). The authors are grateful to Dr. Miodrag Mitrić for XRD measurements.

References

- Abdel-Halim ES, Al-Deyab SS (2011) Removal of heavy metals from their aqueous solutions through adsorption onto natural polymers. *Carbohydr Polym* 84:454–458. doi: 10.1016/j.carbpol.2010.12.001
- Ahmed MA, Ali SM, El-Dek SI, Galal A (2013) Magnetite–hematite nanoparticles prepared by green methods for heavy metal ions removal from water. *Mater Sci Eng B* 178:744–751. doi: 10.1016/j.mseb.2013.03.011
- Bizerea Spiridon O, Pitulice L (2014) Phenol removal from wastewater by adsorption on zeolitic composite. *Environ Sci Pollut Res* (2013) 20:6367–6381. doi: 10.1007/s11356-013-1625-x
- Boehm HP (1994) Some aspects of the surface chemistry of carbon blacks and other carbons. *Carbon N Y* 32:759–769
- Brand R (2008) WinNormos Mössbauer fitting program
- Budimirović D, Veličković ZS, Djokić VR, et al (2017) Efficient As(V) removal by α -FeOOH and α -FeOOH/ α -MnO₂ embedded PEG-6-arm functionalized multiwall carbon nanotubes. *Chem Eng Res Des* 119:75–86. doi: 10.1016/j.cherd.2017.01.010
- Buzatu A, Buzgar N (2010) The Raman study of single-chain silicates. *Analele Stiint ale Univ "Al I Cuza" din Iasi*, *Geol* 56:107–125. doi: 10.13140/2.1.4600.9288
- Capretta A, Maharajh RB, Bell RA (1995) Synthesis and characterization of cyclomaltoheptaose-based metal chelants as probes for intestinal permeability. *Carbohydr Res* 267:49–63. doi: 10.1016/0008-6215(94)00289-R
- Carvalho MD, Henriques F, Ferreira LP, et al (2013) Iron oxide nanoparticles: The influence of synthesis method and size on composition and magnetic properties. *J Solid State Chem* 201:144–152. doi: 10.1016/j.jssc.2013.02.024
- Chen Q, Hills CD, Yuan M, et al (2008) Characterization of carbonated tricalcium silicate and its sorption capacity for heavy metals: A micron-scale composite adsorbent of active silicate gel and calcite. *J Hazard Mater* 153:775–783. doi: 10.1016/j.jhazmat.2007.09.023

- 1
2
3
4 Costa GM, De Grave E, Vandenberghe RE (1998) Mössbauer studies of magnetite and Al-
5 substituted maghemites. *Hyperfine Interact* 117:207–243. doi: 10.1023/A:1012691209853
6
7 D'Halluin M, Rull-Barrull J, Bretel G, et al (2017) Chemically modified cellulose filter paper for
8 heavy metal remediation in water. *ACS Sustain Chem Eng* 5:1965–1973. doi:
9 10.1021/acssuschemeng.6b02768
10
11 da Costa GM (1995) Influence of Nonstoichiometry and the Presence of Maghemite on the
12 Mössbauer Spectrum of Magnetite†. *Clays Clay Miner* 43:656–668. doi:
13 10.1346/CCMN.1995.0430602
14
15 de Faria DLA, Venâncio Silva S, de Oliveira MT (1997) Raman microspectroscopy of some iron
16 oxides and oxyhydroxides. *J Raman Spectrosc* 28:873–878. doi: 10.1002/(SICI)1097-
17 4555(199711)28:11<873::AID-JRS177>3.0.CO;2-B
18
19 Dézsi I, Fetzer C, Gombkötő Á, et al (2008) Phase transition in nanomagnetite. *J Appl Phys*
20 103:104312. doi: 10.1063/1.2937252
21
22 Ding H, Lu SC, Du GX (2011) Surface modification of wollastonite by the mechano-activated
23 method and its properties. *Int J Miner Metall Mater* 18:83–88. doi: 10.1007/s12613-011-
24 0404-2
25
26 Dowty E, Lindsley DH (1973) Mössbauer spectra of synthetic Ca-Fe pyroxenoids and lunar
27 pyroxferroite. *Contrib to Mineral Petrol* 48:229–232. doi: 10.1007/BF00383358
28
29 Dražić A, Tomić NZ, Veličić Z, et al (2017) Highly ordered macroporous γ -alumina prepared by
30 a modified sol-gel method with a PMMA microsphere template for enhanced Pb^{2+} , Ni^{2+} and
31 Cd^{2+} removal. *Ceram Int* 43:13817–13827. doi: 10.1016/j.ceramint.2017.07.102
32
33 Dyar MD, Agresti DG, Schaefer MW, et al (2006) Mössbauer Spectroscopy of Earth and
34 Planetary Materials. *Annu Rev Earth Planet Sci* 34:83–125. doi:
35 10.1146/annurev.earth.34.031405.125049
36
37 Ebbert C, Grundmeier G, Buitkamp N, et al (2014) Toward a microscopic understanding of the
38 calcium–silicate–hydrates/water interface. *Appl Surf Sci* 290:207–214. doi:
39 10.1016/j.apsusc.2013.11.045
40
41 EPA (2014) United State Environmental Protection Agency
42
43 Fock J, Bogart LK, González-Alonso D, et al (2017) On the ‘centre of gravity’ method for
44 measuring the composition of magnetite/maghemite mixtures, or the stoichiometry of
45 magnetite-maghemite solid solutions, via ^{57}Fe Mössbauer spectroscopy. *J Phys D Appl*
46 *Phys* 50:265005. doi: 10.1088/1361-6463/aa73fa
47
48 Gorski CA, Scherer MM (2010) Determination of nanoparticulate magnetite stoichiometry by
49 Mössbauer spectroscopy, acidic dissolution, and powder X-ray diffraction: A critical
50 review. *Am Mineral* 95:1017–1026. doi: 10.2138/am.2010.3435
51
52 Gustafsson JP (2011) Visual MINTEQ. 3.0, beta
53
54
55
56
57
58
59
60
61
62
63
64
65

- 1
2
3
4 Han Q, Chen L, Li W, et al (2018) Self-assembled three-dimensional double network graphene
5 oxide/polyacrylic acid hybrid aerogel for removal of Cu²⁺ from aqueous solution. *Environ*
6 *Sci Pollut Res* 25:34438–34447. doi: 10.1007/s11356-018-3409-9
7
8
9 Haring MM (1942) *The Theory of Rate Processes* (Glasstone, Samuel; Laidler, Keith J.; Eyring,
10 Henry). *J Chem Educ* 19:249. doi: 10.1021/ed019p249.1
11
12 Huang X, Zhan X, Wen C, et al (2017) Amino-functionalized magnetic bacterial
13 cellulose/activated carbon composite for Pb²⁺ and methyl orange sorption from aqueous
14 solution. *J Mater Sci Technol*. doi: 10.1016/j.jmst.2017.03.013
15
16
17 Iannazzo D, Pistone A, Ziccarelli I, et al (2017) Removal of heavy metal ions from wastewaters
18 using dendrimer-functionalized multi-walled carbon nanotubes. *Environ Sci Pollut Res*
19 24:14735–14747. doi: 10.1007/s11356-017-9086-2
20
21
22 Johnston CP, Chrysochoou M (2014) Mechanisms of chromate adsorption on hematite. *Geochim*
23 *Cosmochim Acta* 138:146–175
24
25
26 Joos A, Rügenapp C, Wagner FE, Gleich B (2016) Characterisation of iron oxide nanoparticles
27 by Mössbauer spectroscopy at ambient temperature. *J Magn Magn Mater* 399:123–129. doi:
28 10.1016/j.jmmm.2015.09.060
29
30
31 Kalantari K, Ahmad MB, Masoumi HRF, et al (2014) Rapid adsorption of heavy metals by
32 Fe₃O₄/talc nanocomposite and optimization study using response surface methodology. *Int J*
33 *Mol Sci* 15:12913–12927. doi: 10.3390/ijms150712913
34
35
36 Kalska-Szostko B, Satuła D, Olszewski W (2015) Mössbauer spectroscopy studies of the
37 magnetic properties of ferrite nanoparticles. *Curr Appl Phys* 15:226–231. doi:
38 10.1016/j.cap.2014.12.011
39
40
41 Karnib M, Kabbani A, Holail H, Olama Z (2014) Heavy metals removal using activated carbon,
42 silica and silica activated carbon composite. *Energy Procedia* 50:113–120. doi:
43 10.1016/j.egypro.2014.06.014
44
45
46 Karthikeyan T, Rajgopal S, Miranda LR (2005) Chromium(VI) adsorption from aqueous
47 solution by Hevea Brasilinesis sawdust activated carbon. *J Hazard Mater* 124:192–199. doi:
48 10.1016/j.jhazmat.2005.05.003
49
50
51 Khalil MI (2015) Co-precipitation in aqueous solution synthesis of magnetite nanoparticles using
52 iron(III) salts as precursors. *Arab J Chem* 8:279–284. doi: 10.1016/j.arabjc.2015.02.008
53
54
55 Kumari M, Pittman CU, Mohan D (2015) Heavy metals [chromium(VI) and lead(II)] removal
56 from water using mesoporous magnetite (Fe₃O₄) nanospheres. *J Colloid Interface Sci*
57 442:120–132. doi: 10.1016/j.jcis.2014.09.012
58
59
60 Kündig W, Steven Hargrove R (1969) Electron hopping in magnetite. *Solid State Commun*
61 7:223–227. doi: 10.1016/0038-1098(69)90729-7
62
63
64 Li Y-S, Church JS, Woodhead AL (2012) Infrared and Raman spectroscopic studies on iron
65 oxide magnetic nano-particles and their surface modifications. *J Magn Magn Mater*

1
2
3
4 324:1543–1550. doi: 10.1016/j.jmmm.2011.11.065
5

6 Lin S, Lian C, Xu M, et al (2017) Study on competitive adsorption mechanism among oxyacid-
7 type heavy metals in co-existing system : Removal of aqueous As(V), Cr(III) and As (III)
8 using magnetic iron oxide nanoparticles (MIONPs) as adsorbents. 422:675–681. doi:
9 10.1016/j.apsusc.2017.06.079
10

11 Liu C-H, Chuang Y-H, Chen T-Y, et al (2015) Mechanism of arsenic adsorption on magnetite
12 nanoparticles from water: Thermodynamic and spectroscopic studies. Environ Sci Technol
13 49:7726–7734. doi: 10.1021/acs.est.5b00381
14
15

16 March J (1985) Advanced organic chemistry: Reaction, mechanisms and structure. John Wiley &
17 Sons Inc., New York
18

19 Markovski JS, Đokić V, Milosavljević M, et al (2014a) Ultrasonic assisted arsenate adsorption
20 on solvothermally synthesized calcite modified by goethite, α -MnO₂ and goethite/ α -MnO₂.
21 Ultrason Sonochem 21:790–801. doi: 10.1016/j.ultsonch.2013.10.006
22
23

24 Markovski JS, Marković DD, Dokić VR, et al (2014b) Arsenate adsorption on waste eggshell
25 modified by goethite, α -MnO₂ and goethite/ α -MnO₂. Chem Eng J 237:430–442. doi:
26 10.1016/j.cej.2013.10.031
27
28

29 Martin S, Griswold W (2009) Human health effects of heavy metals. Cent. Hazard. Subst. Res.
30 Environmental Sci. Technol. Briefs Citizens 1–6
31

32 Mezenner NY, Bensmaili A (2009) Kinetics and thermodynamic study of phosphate adsorption
33 on iron hydroxide-eggshell waste. Chem Eng J 147:87–96. doi: 10.1016/j.cej.2008.06.024
34

35 Murad E, Wagner U (1998) Clays and clay minerals: The firing process. Hyperfine Interact
36 117:337–356. doi: 10.1023/A:1012683008035
37
38

39 Obradović N, Filipović S, Marković S, et al (2017a) Influence of different pore-forming agents
40 on wollastonite microstructures and adsorption capacities. Ceram Int 43:7461–7468. doi:
41 10.1016/j.ceramint.2017.03.021
42

43 Obradović N, Filipović S, Rusmirović J, et al (2017b) Formation of porous wollastonite-based
44 ceramics after sintering with yeast as the pore-forming agent. Sci Sinter 49:. doi:
45 10.2298/SOS1703235O
46
47

48 Oshtrakh MI, Ushakov MV, Šepelák V, et al (2016) Study of iron oxide nanoparticles using
49 Mössbauer spectroscopy with a high velocity resolution. Spectrochim Acta Part A Mol
50 Biomol Spectrosc 152:666–679. doi: 10.1016/j.saa.2015.06.017
51
52

53 Osticioli I, Mendes NFC, Nevin A, et al (2009) Analysis of natural and artificial ultramarine blue
54 pigments using laser induced breakdown and pulsed Raman spectroscopy, statistical
55 analysis and light microscopy. Spectrochim Acta Part A Mol Biomol Spectrosc 73:525–
56 531. doi: 10.1016/j.saa.2008.11.028
57

58 Ovsyannikov S V., Shchennikov V V., Shvetsova MA, et al (2010) Tuning of the stoichiometry
59 of of Fe_{1-x}O wüstite by compression wüstite by compression. Phys Rev B 81:060101. doi:
60
61
62
63
64
65

1
2
3
4 10.1103/PhysRevB.81.060101
5

6 Paul D (2017) Research on heavy metal pollution of river Ganga: A review. *Ann Agrar Sci*
7 15:278–286. doi: 10.1016/j.aasci.2017.04.001
8

9
10 Petrova TM, Fachikov L, Hristov J (2011) The magnetite as adsorbent for some hazardous
11 species from aqueous solution: A review. *Int Rev Chem Eng Int Rev Chem Eng* 3:134–152
12

13 Qi Z, Joshi TP, Liu R, et al (2017) Synthesis of Ce(III)-doped Fe₃O₄ magnetic particles for
14 efficient removal of antimony from aqueous solution. *J Hazard Mater* 329:193–204. doi:
15 10.1016/j.jhazmat.2017.01.007
16

17 Qiu H, Lv L, Pan B, et al (2009) Critical review in adsorption kinetic models. *J Zhejiang Univ*
18 *Sci A* 10:716–724. doi: 10.1631/jzus.A0820524
19

20
21 Rajput S, Pittman CU, Mohan D (2016) Magnetic magnetite (Fe₃O₄) nanoparticle synthesis and
22 applications for lead (Pb²⁺) and chromium (Cr⁶⁺) removal from water. *J Colloid Interface*
23 *Sci* 468:334–346. doi: 10.1016/j.jcis.2015.12.008
24

25 Razzaque MS (2011) Phosphate toxicity: new insights into an old problem. *Clin Sci* 120:91–97.
26 doi: 10.1042/CS20100377
27

28 Ricciardi P, Colomban P, Tournié A, Milande V (2009) Nondestructive on-site identification of
29 ancient glasses: genuine artefacts, embellished pieces or forgeries? *J Raman Spectrosc*
30 40:604–617. doi: 10.1002/jrs.2165
31

32
33 Richet P, Mysen BO, Ingrin J (1998) High-temperature X-ray diffraction and Raman
34 spectroscopy of diopside and pseudowollastonite. *Phys Chem Miner* 25:401–414. doi:
35 10.1007/s002690050130
36

37 Roggwiler P, Kundig W (1973) Mössbauer spectra of superparamagnetic Fe₃O₄. *Differentiation*
38 12:901–903
39

40
41 Rouquerol F, Rouquerol J, Sing, Kenneth (1999) Adsorption by powders and porous solids:
42 Principles, methodology and application. Academic Press, USA
43

44 Rout PR, Bhunia P, Dash RR (2015) Effective utilization of a sponge iron industry by-product
45 for phosphate removal from aqueous solution: A statistical and kinetic modelling approach.
46 *J Taiwan Inst Chem Eng* 46:98–108. doi: 10.1016/j.jtice.2014.09.006
47

48
49 Rout PR, Dash RR, Bhunia P (2016) Nutrient removal from binary aqueous phase by dolochar :
50 Highlighting optimization, single and binary adsorption isotherms and nutrient release.
51 *Process Saf Environ Prot* 100:91–107. doi: 10.1016/j.psep.2016.01.001
52

53 Sarin VK, Kent SBH, Tam JP, Merrifield RB (1981) Quantitative monitoring of solid-phase
54 peptide synthesis by the ninhydrin reaction. *Anal Biochem* 117:147–157. doi:
55 10.1016/0003-2697(81)90704-1
56

57
58 Sellaoui L, Bouzid M, Duclaux L, et al (2016a) Binary adsorption isotherms of two ionic liquids
59 and ibuprofen on an activated carbon cloth: simulation and interpretations using a statistical
60
61
62
63
64
65

1
2
3
4 and COSMO-RS models. RSC Adv 6:67701–67714. doi: 10.1039/C6RA03405E
5

6 Sellaoui L, Dotto GL, Goncalves JO, et al (2016b) Equilibrium modeling of single and binary
7 adsorption of Food Yellow 4 and Food Blue 2 on modified chitosan using a statistical
8 physics theory: new microscopic interpretations. J Mol Liq 222:151–158. doi:
9 10.1016/j.molliq.2016.07.005
10

11
12 Sellaoui L, Dotto GL, Lamine A Ben, Erto A (2017a) Interpretation of single and competitive
13 adsorption of cadmium and zinc on activated carbon using monolayer and exclusive
14 extended monolayer models. Environ Sci Pollut Res 24:19902–19908. doi: 10.1007/s11356-
15 017-9562-8
16

17
18 Sellaoui L, Edi Soetaredjo F, Ismadji S, et al (2017b) New insights into single-compound and
19 binary adsorption of copper and lead ions on treated sea mango shell: Experimental and
20 theoretical studies. Phys Chem Chem Phys 19:25927–25937. doi: 10.1039/c7cp03770h
21

22
23 Sharma YC (2001) Adsorption of Cr(VI) onto wollastonite: Effect of pH. Indian J Chem Technol
24 8:186–190
25

26
27 Sharma YC, Gupta GS, Prasad G, Rupainwar DC (1990a) Use of wollastonite in the removal of
28 Ni(II) from aqueous solutions. Water Air Soil Pollut 49:69–79. doi: 10.1007/BF00279511
29

30
31 Sharma YC, Prasad G, Rupainwar DI (1990b) Adsorption for removal of Cd(II) from effluents.
32 Int J Environ Stud 36:315–320. doi: 10.1080/00207239008710609
33

34
35 Sharma YC, Uma, Srivastava V, et al (2007) Reclamation of Cr(VI) rich water and wastewater
36 by wollastonite. Chem Eng J 127:151–156. doi: 10.1016/j.cej.2006.09.012
37

38
39 Shim SE, Kim K, Oh S, Choe S (2004) Preparation of ultra fine poly(methyl methacrylate)
40 microspheres in methanol-enriched aqueous medium. Macromol Res 12:240–245. doi:
41 10.1007/BF03218394
42

43
44 Sokol E V., Seryotkin Y V., Kokh SN, et al (2015) Flamite, $(Ca,Na,K)_2(Si,P)O_4$, a new mineral
45 from ultrahightemperature combustion metamorphic rocks, Hatrurim Basin, Negev Desert,
46 Israel. Mineral Mag 79:583–596. doi: 10.1180/minmag.2015.079.3.05
47

48
49 Sreekanth Chakradhar RP, Nagabhushana BM, Chandrappa GT, et al (2006) Solution
50 combustion derived nanocrystalline macroporous wollastonite ceramics. Mater Chem Phys
51 95:169–175. doi: 10.1016/j.matchemphys.2005.06.002
52

53
54 Stevens JG, Khasanov AM, Miller JW, et al (2005) Mössbauer Mineral Handbook. The
55 University of North Carolina at Asheville
56

57
58 Suzdalev IP, Maksimov Y V., Buravtsev VN, et al (2012) Magnetic properties of monodisperse
59 nanomagnetite. Russ J Phys Chem B 6:163–168. doi: 10.1134/S1990793112010228
60

61
62 Swamy V, Dubrovinsky LS, Tutti F (1997) High-temperature raman spectra and thermal
63 expansion of wollastonite. J Am Ceram Soc 80:2237–2247. doi: 10.1111/j.1151-
64 2916.1997.tb03113.x
65

- 1
2
3
4 Taleb K, Markovski J, Milosavljević M, et al (2015) Efficient arsenic removal by cross-linked
5 macroporous polymer impregnated with hydrous iron oxide: Material performance. *Chem*
6 *Eng J* 279:.. doi: 10.1016/j.cej.2015.04.147
7
8
9 Taleb K, Markovski J, Veličković Z, et al (2016a) Arsenic removal by magnetite-loaded amino
10 modified nano/microcellulose adsorbents: Effect of functionalization and media size. *Arab J*
11 *Chem*. doi: 10.1016/j.arabjc.2016.08.006
12
13 Taleb KA, Rusmirović JD, Rančić MP, et al (2016b) Efficient pollutants removal by amino-
14 modified nanocellulose impregnated with iron oxide. *J Serbian Chem Soc* 81:.. doi:
15 10.2298/JSC160529063T
16
17
18 Tejedor-Tejedor MI, Anderson MA (1990) The protonation of phosphate on the surface of
19 goethite as studied by CIR-FTIR and electrophoretic mobility. *Langmuir* 6:602–611. doi:
20 10.1021/la00093a015
21
22 Veličković Z, Vuković GD, Marinković AD, et al (2012) Adsorption of arsenate on iron(III)
23 oxide coated ethylenediamine functionalized multiwall carbon nanotubes. *Chem Eng J* 181–
24 182:174–181. doi: 10.1016/j.cej.2011.11.052
25
26 Vuković GD, Marinković AD, Čolić M, et al (2010) Removal of cadmium from aqueous
27 solutions by oxidized and ethylenediamine-functionalized multi-walled carbon nanotubes.
28 *Chem Eng J* 157:238–248. doi: 10.1016/j.cej.2009.11.026
29
30
31 Vuković GD, Marinković AD, Škapin SD, et al (2011) Removal of lead from water by amino
32 modified multi-walled carbon nanotubes. *Chem Eng J* 173:855–865. doi:
33 10.1016/j.cej.2011.08.036
34
35
36 Wang X, Mao H, Huang W, et al (2011) Preparation of magnetic imprinted polymer particles via
37 microwave heating initiated polymerization for selective enrichment of 2-amino-4-
38 nitrophenol from aqueous solution. *Chem Eng J* 178:85–92. doi: 10.1016/j.cej.2011.10.015
39
40 Wang Y, Li B, Zhou Y, Jia D (2009) In situ mineralization of magnetite nanoparticles in
41 chitosan hydrogel. *Nanoscale Res Lett* 4:1041–1046. doi: 10.1007/s11671-009-9355-1
42
43 White SN (2009) Laser Raman spectroscopy as a technique for identification of seafloor
44 hydrothermal and cold seep minerals. *Chem Geol* 259:240–252. doi:
45 10.1016/j.chemgeo.2008.11.008
46
47
48 Zach-Maor A, Semiat R, Shemer H (2011) Adsorption–desorption mechanism of phosphate by
49 immobilized nano-sized magnetite layer: Interface and bulk interactions. *J Colloid Interface*
50 *Sci* 363:608–614. doi: 10.1016/j.jcis.2011.07.062
51
52
53 Zeng B, Yang L, Zheng W, et al (2017) Analysis of the formation process and performance of
54 magnetic Fe₃O₄@Poly(4-vinylpyridine) absorbent prepared by in-situ synthesis. *J Mater Sci*
55 *Technol* In press,.: doi: 10.1016/j.jmst.2017.07.007
56
57
58 Zeng L, Chen Y, Zhang Q, et al (2015) Adsorption of Cd(II), Cu(II) and Ni(II) ions by cross-
59 linking chitosan/rectorite nano-hybrid composite microspheres. *Carbohydr Polym* 130:333–
60 43. doi: 10.1016/j.carbpol.2015.05.015
61
62
63
64
65

1
2
3
4 Zhao J, Zhu YJ, Wu J, et al (2014) Chitosan-coated mesoporous microspheres of calcium silicate
5 hydrate: Environmentally friendly synthesis and application as a highly efficient adsorbent
6 for heavy metal ions. J Colloid Interface Sci 418:208–215. doi: 10.1016/j.jcis.2013.12.016
7
8
9

10 **Figure Caption**

11
12
13
14 **Fig. 1.** Schematic illustration of 1) direct attaching of MG spheres on WL and 2) attaching of
15 MG spheres on amino/carboxylic acid functionalized WL
16

17 **Fig. 2.** ATR-FTIR spectra of modified wollastonite based adsorbents

18
19 **Fig. 3.** Raman spectra of W-MG and W- γ -APS/MG adsorbents

20
21 **Fig. 4.** XRD patterns of unmodified WL, WL/MG and WL- γ -APS/MG samples

22
23
24 **Fig. 5.** Room temperature Mössbauer spectrum of the a) WL/MG and b) WL- γ -APS/MG. (On each
25 individual plot, experimental data are presented by solid circles and the fit is given by the red solid line. Vertical
26 arrow denotes relative position of the lowermost peak with respect to the basal line. Red solid line in the lower part
27 of the plot represents the error calculated as the difference (Th-Exp). a) The fitted lines of the Mössbauersubspectra
28 are plotted above the main spectrum fit: D-subspectrum (blue) and B-subspectrum (orange). The largest value of the
29 absolute difference is less than 0.2 %. b) The largest value of the absolute difference is less than 0.09 %.)
30

31 **Fig. 6.** The quadrupole splitting distribution $P(\Delta)$ of the WL- γ -APS/MG sample

32
33 **Fig. 7.** Black line – hyperfine magnetic field distribution $P(B_{\text{hf}})$ of the magnetic part of the
34 WL/MG spectra. Red line - fit of the $P(B_{\text{hf}})$ distribution with five Gaussian (five blue lines)

35
36
37 **Fig. 8.** SEM micrograph of synthesized a) PMMA microsphere, b) unmodified WL, c) WL/MG
38 and d) WL- γ -APS/MG

39
40 **Fig. 9.** EDS mapping of modified WL based adsorbents a) WL/MG and d) WL- γ -APS/MG
41
42
43
44
45
46
47
48
49
50
51
52
53
54
55
56
57
58
59
60
61
62
63
64
65



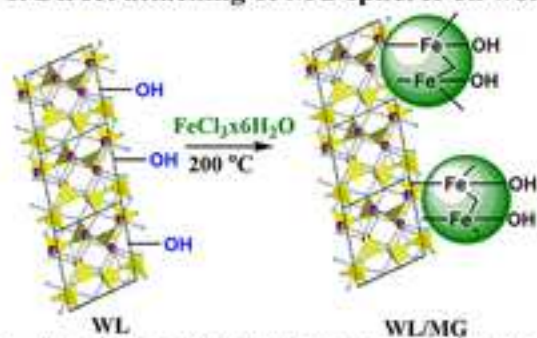
[Click here to access/download](#)

Supplementary Material

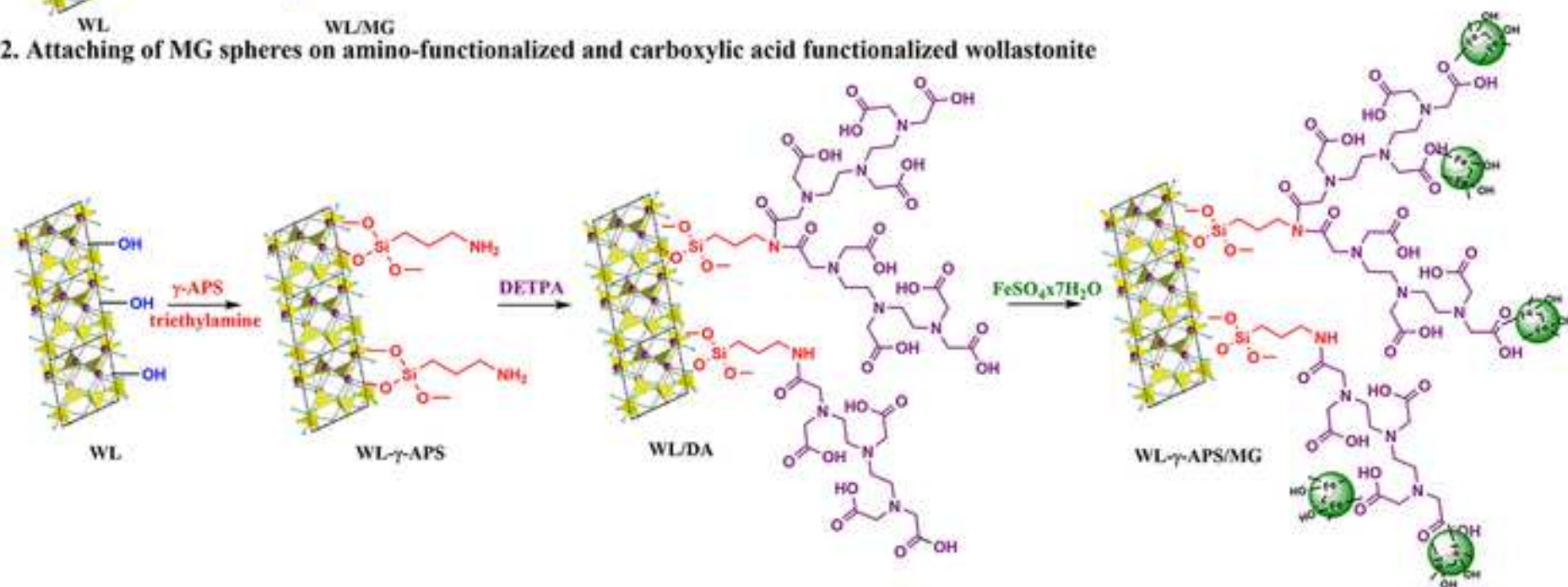
Rusmirovic et al _Supplementary material Revised.docx

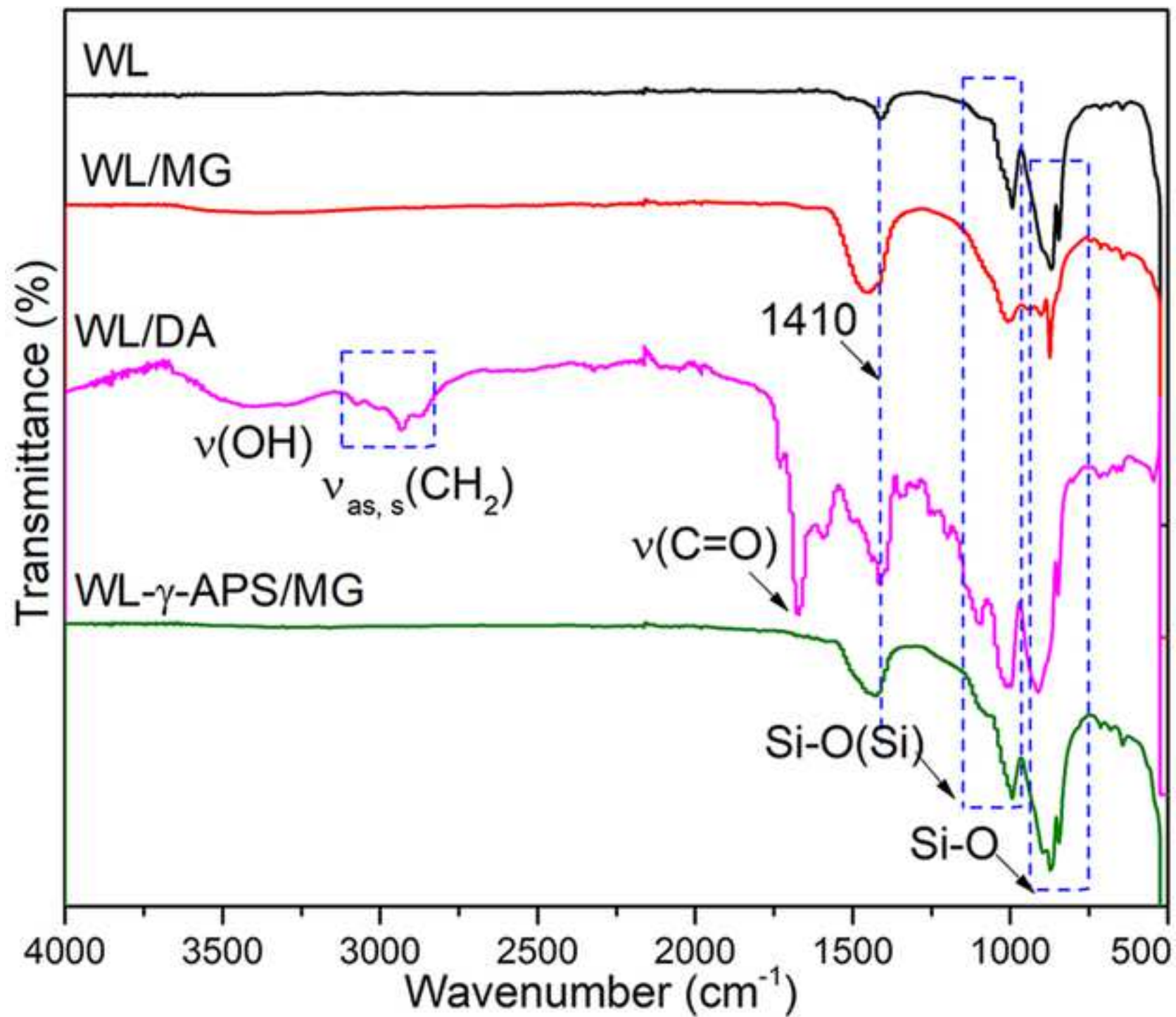


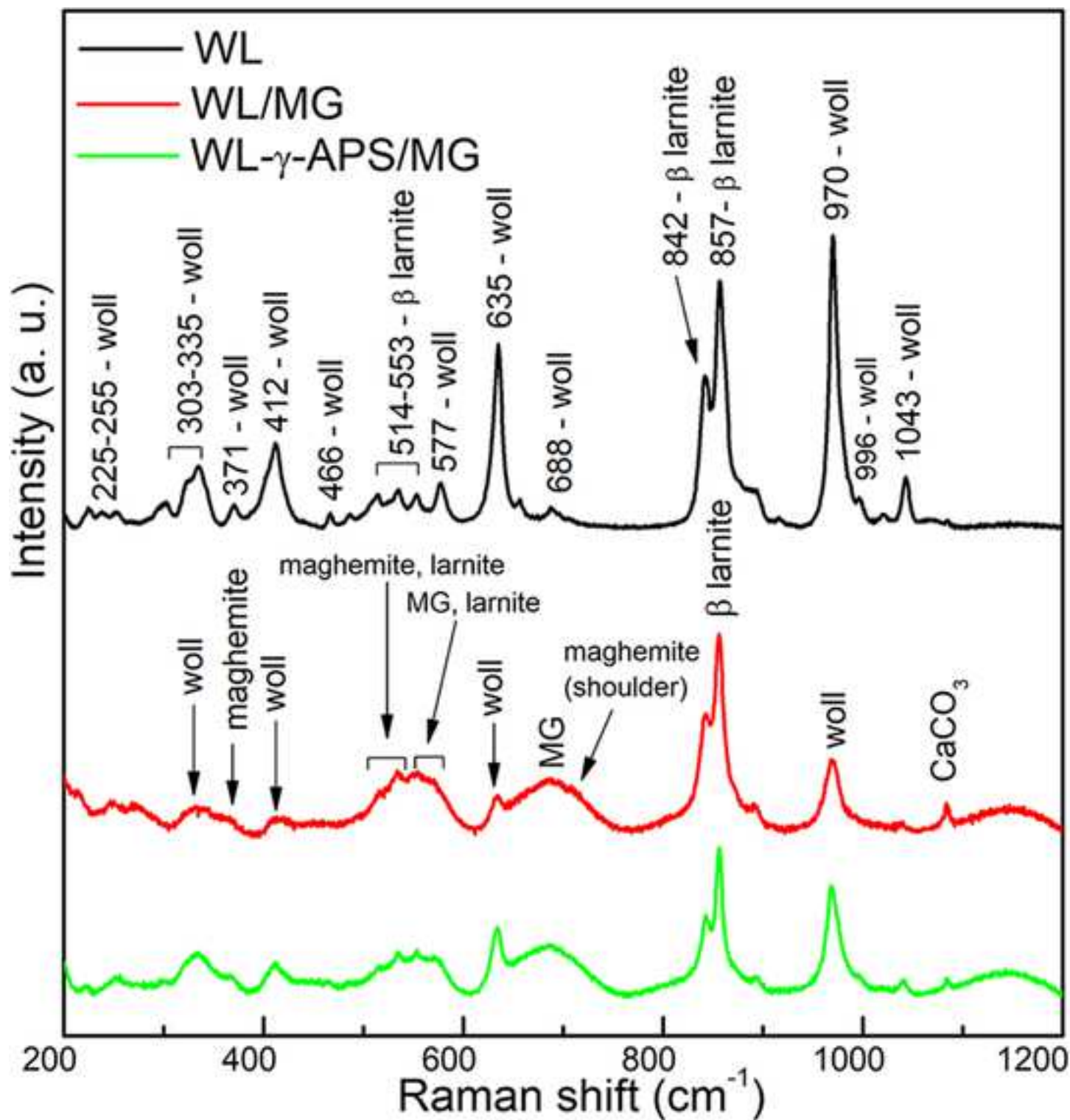
1. Direct attaching of MG spheres on wollastonite

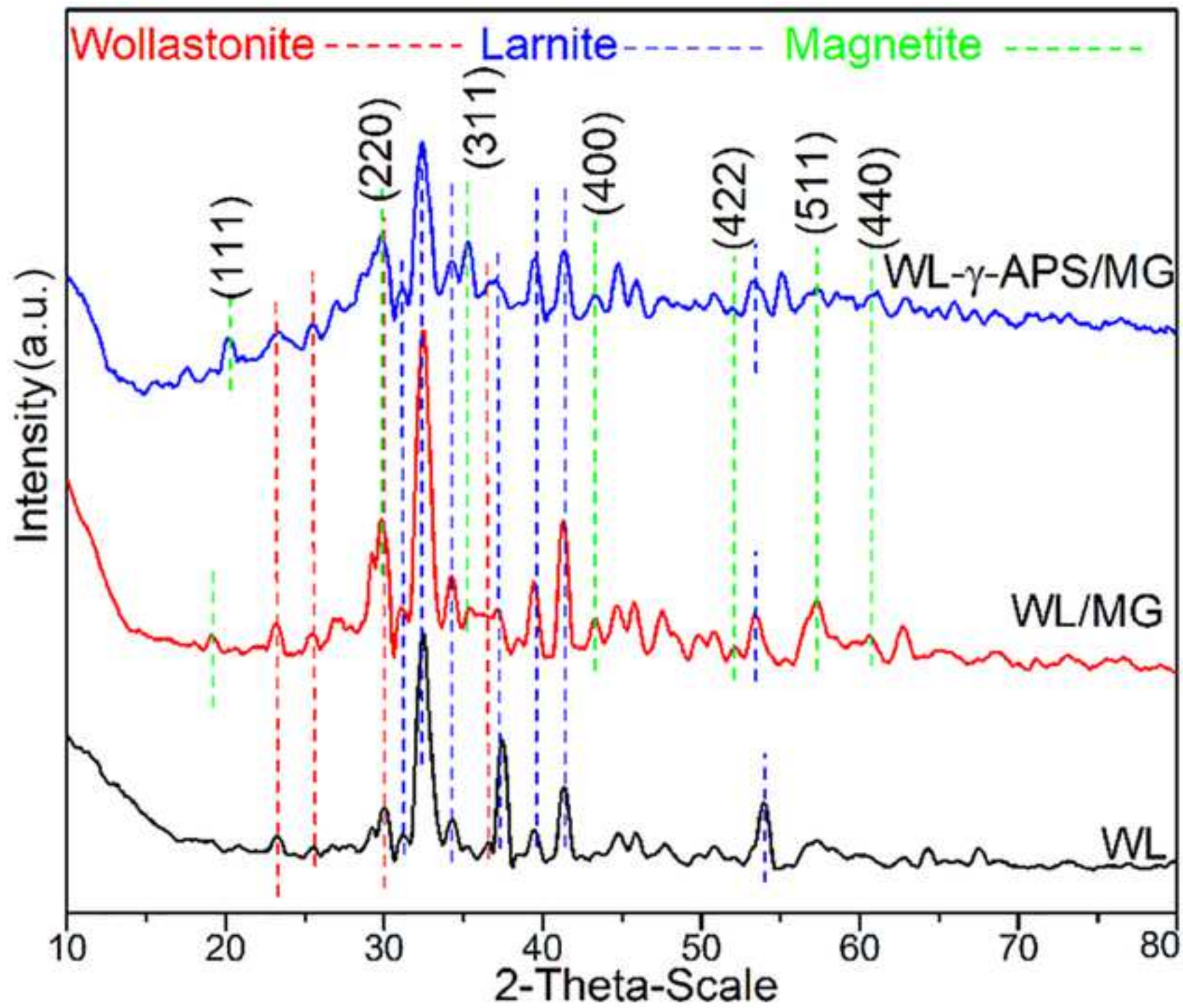


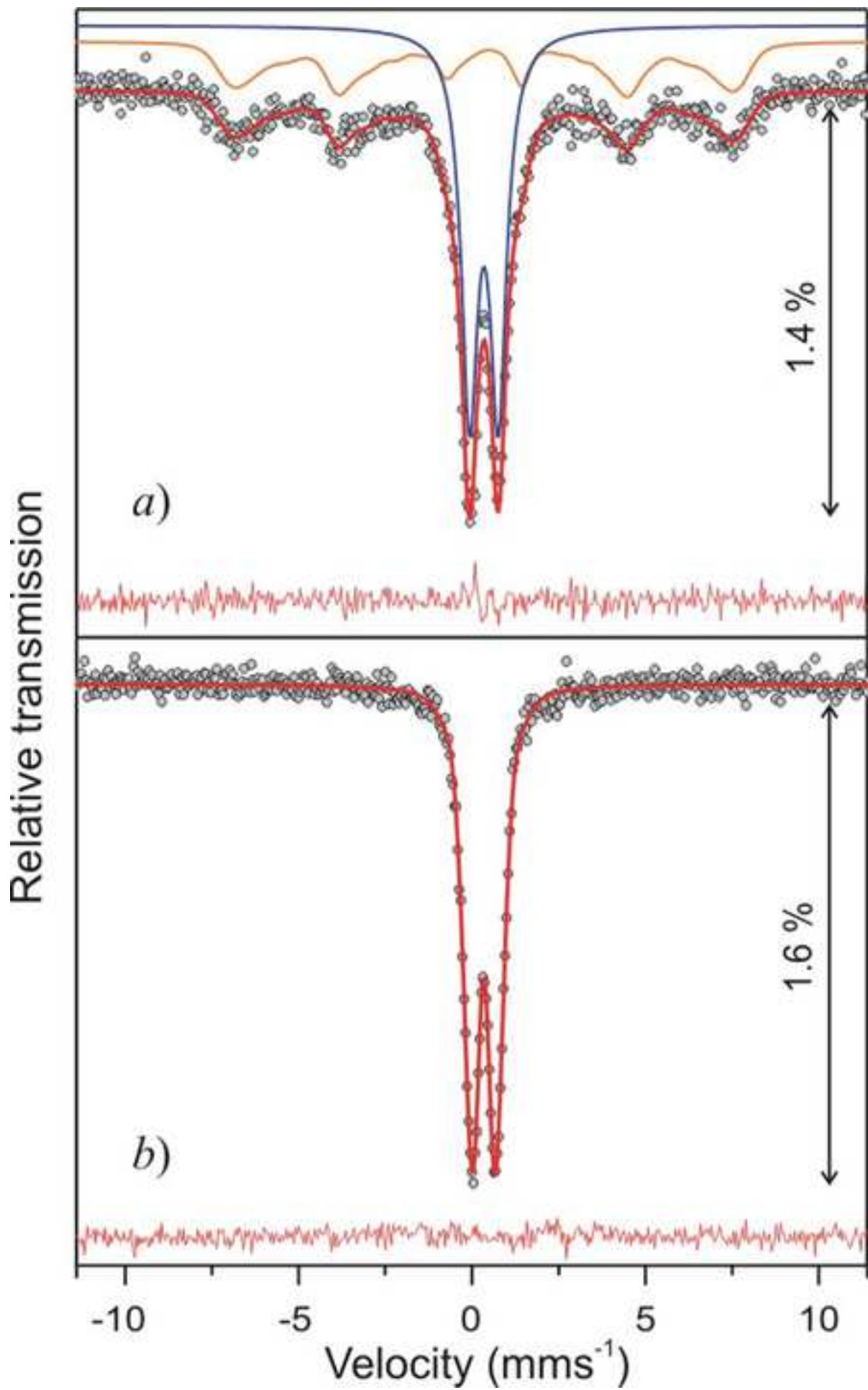
2. Attaching of MG spheres on amino-functionalized and carboxylic acid functionalized wollastonite

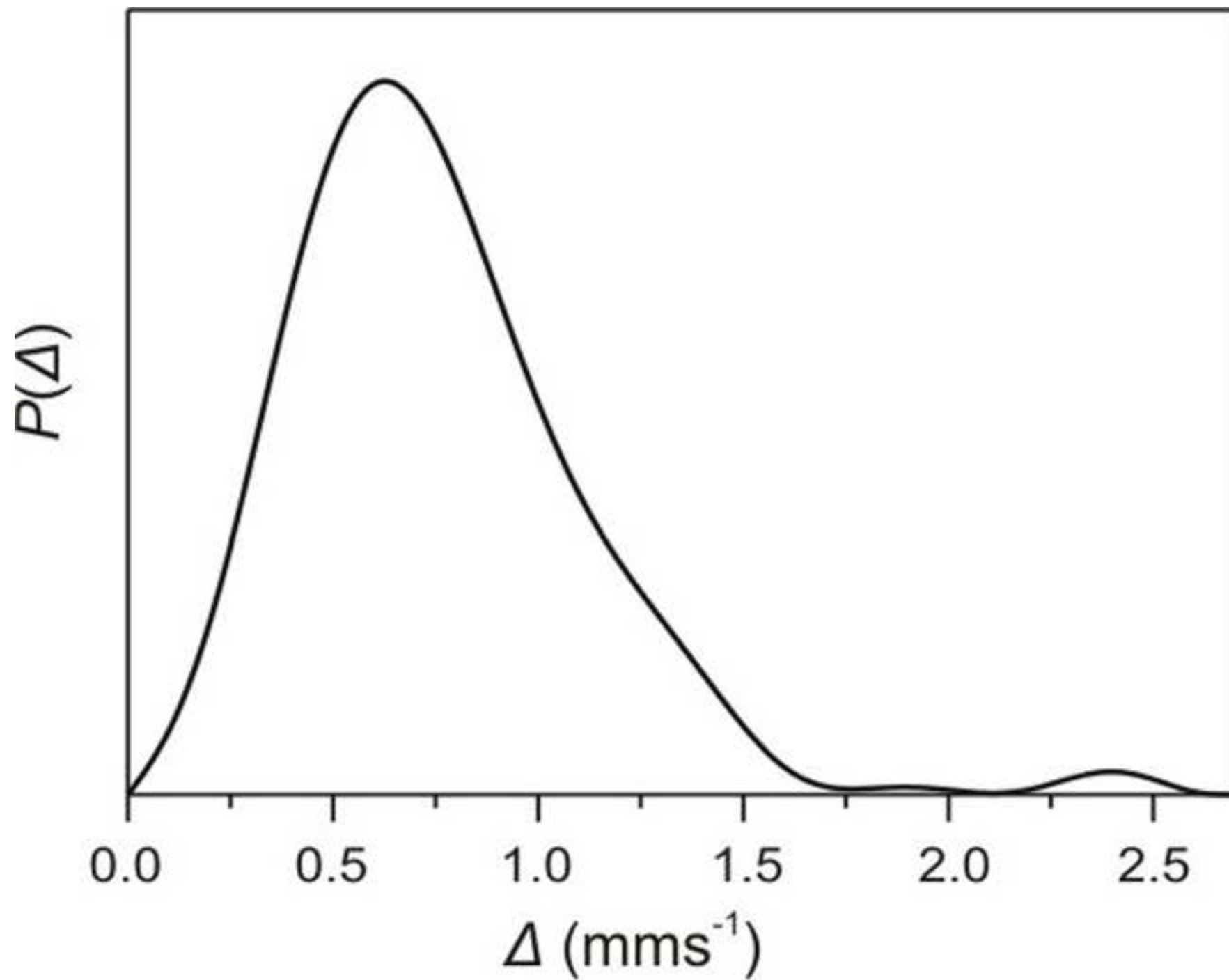


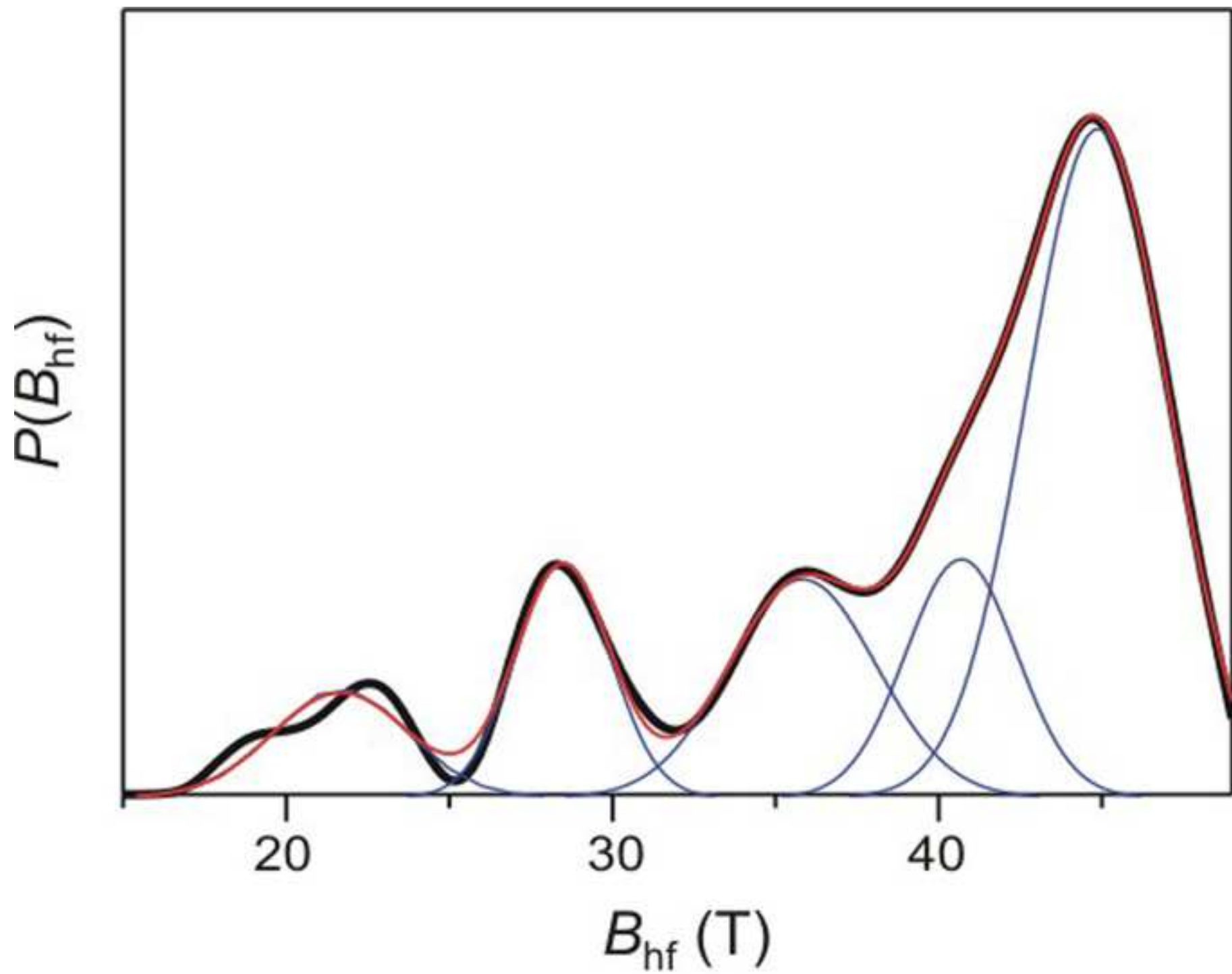


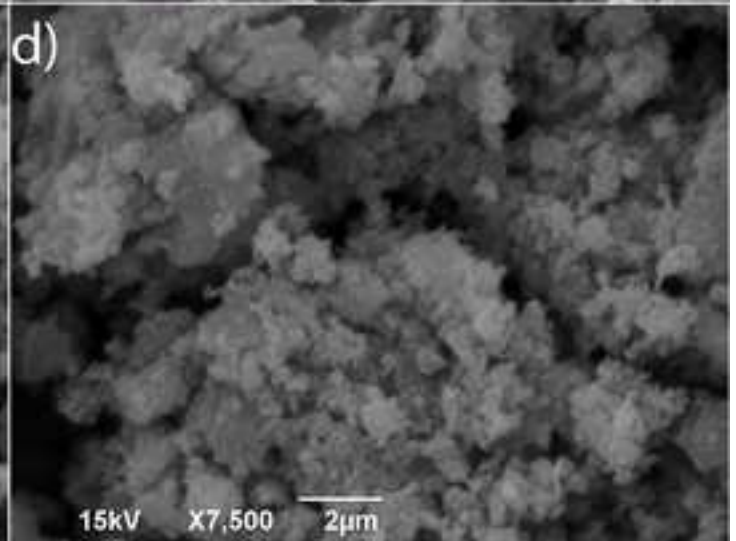
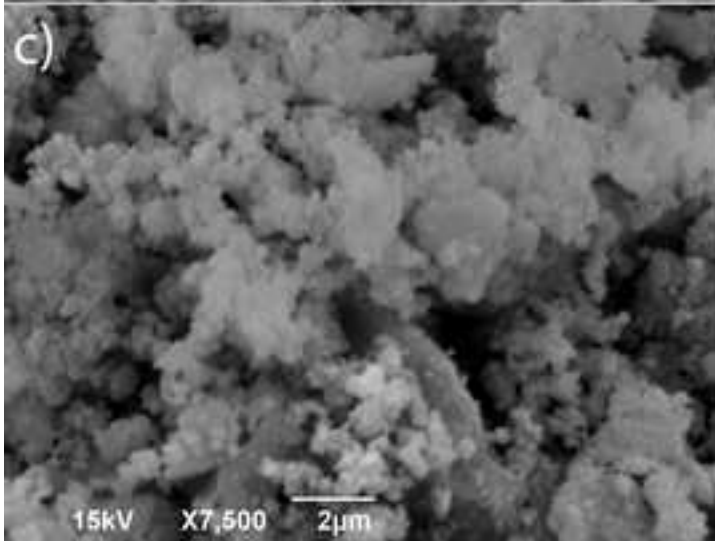
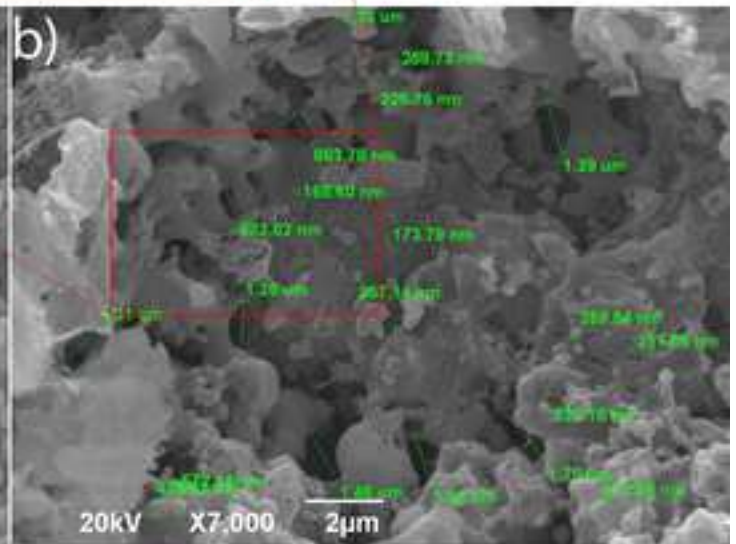
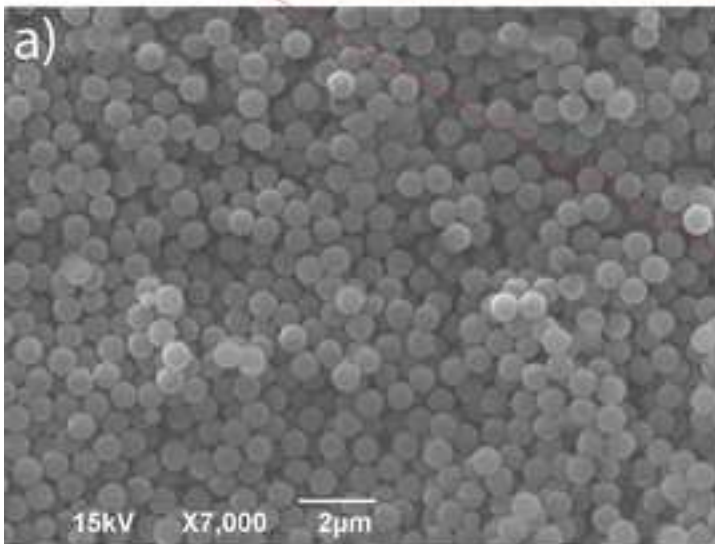
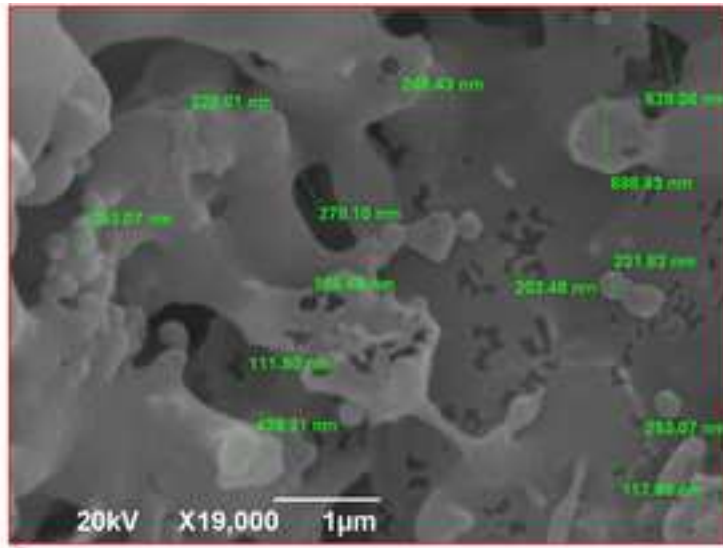












Ref.: Ms. No. ESPR-D-18-08952R1

Controllable Synthesis of Fe₃O₄ -Wollastonite Adsorbents for Efficient Heavy Metal Ions/Oxyanions Removal Environmental Science and Pollution Research

Reviewers' comments:

Reviewer #1: The authors have tried their level best to address the issues raised by the reviewers. They have modified the manuscript extensively incorporating all the reviewer's suggestions. So the reviewer accepts the revised manuscript and recommends for its possible publication in the Journal of Environmental Science and Pollution Research.

Answer: Authors are very grateful for the reviewers' recommendation.

Reviewer #2: Dear editor and authors,

The paper was improved, but this version is not adequate for publication for these reasons:

1. Please review the English Language in the last part of the paper.

Answer: According to the reviewer advice, the last part of the Manuscript is grammar and spell checked by recommended English speaker.

2 The calculation of adsorption energy through statistical physics model is not correct. Please check the references. Thank you

Answer: According to the reviewer advice, the new method is used for the calculation of adsorption energy. Adsorption energy is calculated according to the following equation

$$\varepsilon = k_B T \ln \left(\frac{c_s}{c_{1/2}} \right)$$
, presented in the recommended literature references (Sellaoui et al., Phys.

Chem. Chem. Phys. 2017,19, 25927-25937 and Sellaoui et al., Env-Sci and Pollution Research, 2017, 24,19902–19908). The corrected values of the adsorption energy and of the corresponding parameters (density of receptor site and number of ions that interact with one receptor site) are presented in Table 5.

Reviewer #3: -